Electronic Supplementary Material (ESI) for Journal of Materials Chemistry A.
This journal is © The Royal Society of Chemistry 2022

Electronic Supplementary Information (ESI) for

Experimental Correlation of Mn^{3+} Cation Defects and ORR Electrocatalytic Activity of α–MnO_2 – An X-Ray Photoelectron Spectroscopy Study

Michael F. Fink,*[ac] Morten Weiss,[b] Roland Marschall,[bc] and Christina Roth[ac]

[a]*Chair of Electrochemical Process Engineering, Faculty of Engineering Science, University of Bayreuth, Universitätsstrasse 30, 95447 Bayreuth, Germany.*

[b]*Department of Chemistry, Physical Chemistry III, University of Bayreuth, Universitätsstrasse 30, 95447 Bayreuth, Germany.*

[c]*Bavarian Center for Battery Technology (BayBatt), University of Bayreuth, Universitätsstrasse 30, 95447 Bayreuth, Germany.*

*Corresponding author
Email: michael.fink@uni-bayreuth.de (Michael F. Fink)

Contents of this file

Section S1. Additional SEM images of as-synthesized α-MnO_2

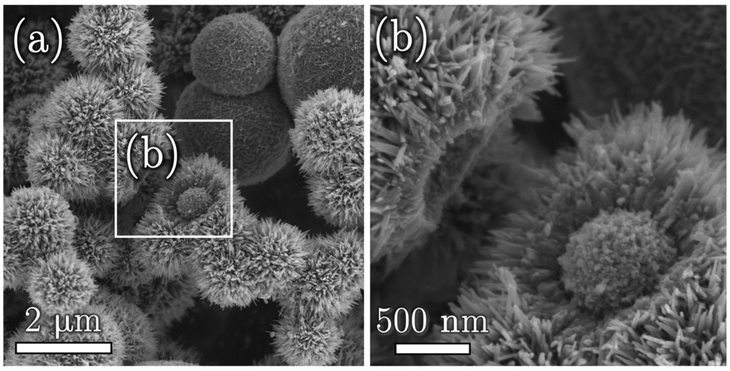

Figure S1. Additional SEM images of α-MnO_2 synthesized at 60°C/8h. (a) Overview of secondary particles and (b) at higher magnification showing a sea-urchin where the spine-shell has come off the microsphere-core.

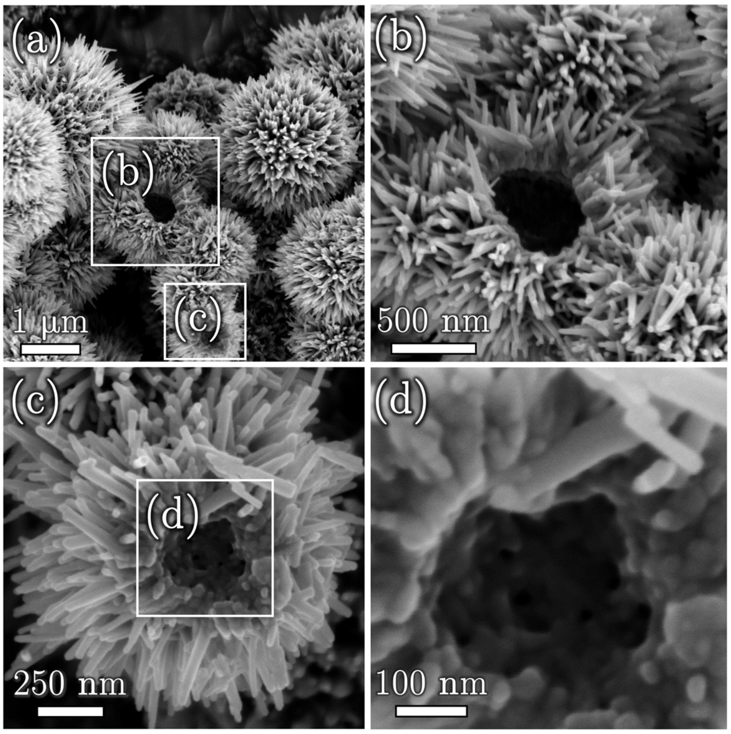

Figure S2. Additional SEM images of α-MnO_2 synthesized at 80°C/4 h. (a) Overview of secondary particles, (b), (c) and (d) higher magnification SEM images of broken sea-urchins revealing a hollow inner core.

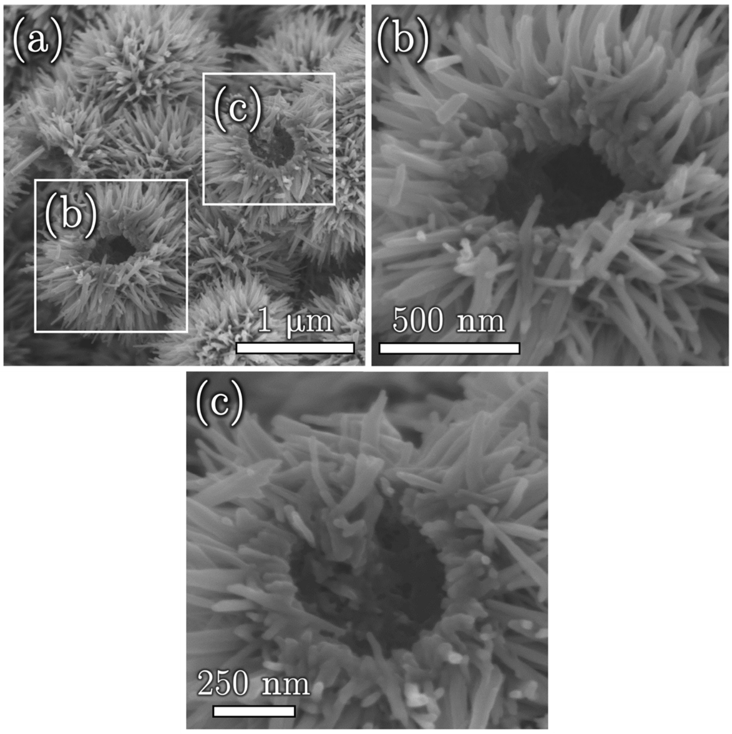

Figure S3. Additional SEM images of α-MnO_2 synthesized at 80°C/8h. (a) Overview of secondary particles, (b) and (c) higher magnification SEM images of broken sea-urchins revealing a hollow inner core.

Section S2. Additional PXRD data of as-synthesized α-MnO$_2$

Table S1. Summarized angular positions of (2 1 1) ($2\theta_{(2\,1\,1)}$) and (6 0 0) crystallographic planes ($2\theta_{(6\,0\,0)}$) as well as calculated *d*-spacings and lattice parameters $a=b$ and c of as-synthesized α-MnO$_2$.

α-MnO$_2$	$2\theta_{(2\,1\,1)}$	$2\theta_{(6\,0\,0)}$	d[a]	$a=b$[b]	c[b]
T/t	°	°	Å	Å	Å
40°C/4h	37.75	56.09	2.38	9.83	2.83
40°C/8h	37.75	56.12	2.38	9.83	2.83
40°C/16h	37.68	55.99	2.39	9.85	2.85
60°C/4h	37.71	56.10	2.38	9.83	2.84
60°C/8h	37.67	56.03	2.39	9.84	2.84
60°C/16h	37.77	56.24	2.38	9.81	2.83
80°C/4h	37.81	56.35	2.38	9.79	2.83
80°C/8h	37.62	56.16	2.39	9.82	2.85
80°C/1h6	37.73	56.16	2.38	9.82	2.84

[a] $d=\frac{n\,\lambda_{\mathrm{CuK}\alpha}}{2\ \sin\theta_{(2\,1\,1)}}$, $n=1$, $\lambda_{\mathrm{CuK}\alpha}=1.4506$ Å[1]

[b] $\frac{1}{d_{\mathrm{h\,k\,l}}}=\frac{\mathrm{h}^2+\mathrm{k}^2}{a^2}+\frac{\mathrm{l}^2}{c^2}$[2,3]

Section S3. SEM-EDX and XPS elemental analysis of as-synthesized α-MnO$_2$

Section S3.1. SEM-EDX

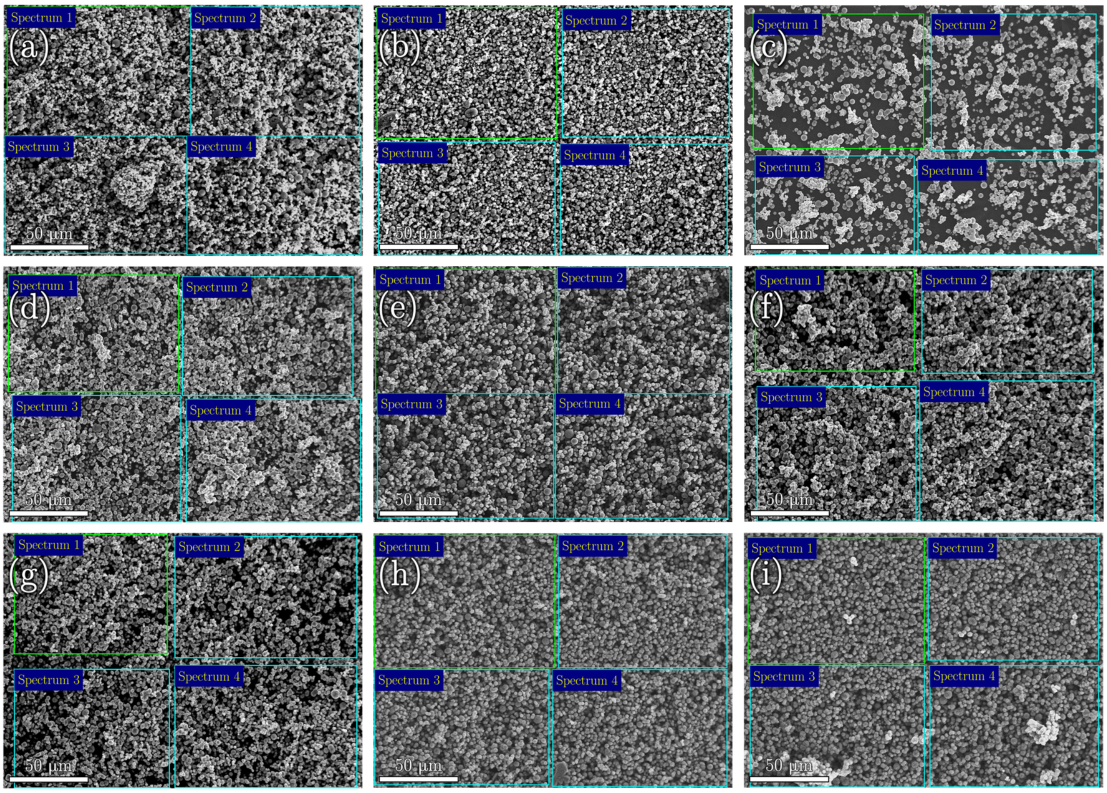

Figure S4. SEM-EDX area analysis of as-synthesized α-MnO$_2$ at 500x magnification and 15 kV acceleration voltage. (a) 40°C/4h, (b) 40°C/8h, (c) 40°C/16h, (d) 60°C/4h, (e) 60°C/8h, (f) 60°C/16h, (g) 80°C/4h, (h) 80°C/80 and (i) 80°C/16h. Green and cyan squares mark the areas where EDX was carried out.

Table S2. Summarized elemental compositions of Mn, O, K and Ag as obtained from SEM-EDX area analysis of as-synthesized α-MnO_2 at 500x magnification and 15 kV acceleration voltage (**Figure S4**). C was deducted from EDX spectra as carbon sputter coating was applied for preparing the samples and the samples were fixed on carbon tabs.

α-MnO_2	Spectrum 1				Spectrum 2				Spectrum 3				Spectrum 4			
T/t	Mn at.-%	O at.-%	K at.-%	Ag at.-%	Mn at.-%	O at.-%	K at.-%	Ag at.-%	Mn at.-%	O at.-%	K at.-%	Ag at.-%	Mn at.-%	O at.-%	K at.-%	Ag at.-%
40°C/4h	45.77	53.00	0.65	0.58	44.68	54.01	0.67	0.64	50.68	48.09	0.65	0.58	46.87	51.89	0.68	0.56
40°C/8h	38.01	60.57	0.86	0.56	36.41	62.08	0.92	0.51	36.90	61.65	0.91	0.54	37.43	61.05	0.97	0.56
40°C/16h	34.90	63.35	1.22	0.54	34.25	63.97	1.36	0.41	36.63	61.52	1.45	0.39	35.24	62.92	1.43	0.41
60°C/4h	41.07	56.89	1.53	0.52	40.01	58.28	1.24	0.47	41.08	56.83	1.57	0.52	41.97	56.09	1.46	0.48
60°C/8h	45.95	51.74	1.79	0.52	45.77	51.98	1.75	0.50	43.99	53.85	1.75	0.41	43.21	54.57	1.74	0.48
60°C/16h	41.56	55.61	2.39	0.44	43.03	53.95	2.51	0.51	43.05	54.18	2.35	0.42	42.39	54.38	2.60	0.63
80°C/4h	38.71	57.53	2.89	0.87	37.62	59.19	2.42	0.77	37.33	59.16	2.85	0.67	38.83	57.78	2.62	0.76
80°C/8h	37.66	59.19	2.50	0.66	36.94	59.91	2.50	0.64	37.71	59.01	2.61	0.67	36.69	59.80	2.82	0.69
80°C/16h	39.28	57.41	2.57	0.74	39.20	57.30	2.68	0.83	39.99	56.66	2.65	0.70	40.85	55.56	2.87	0.72

Section S3.2. XPS

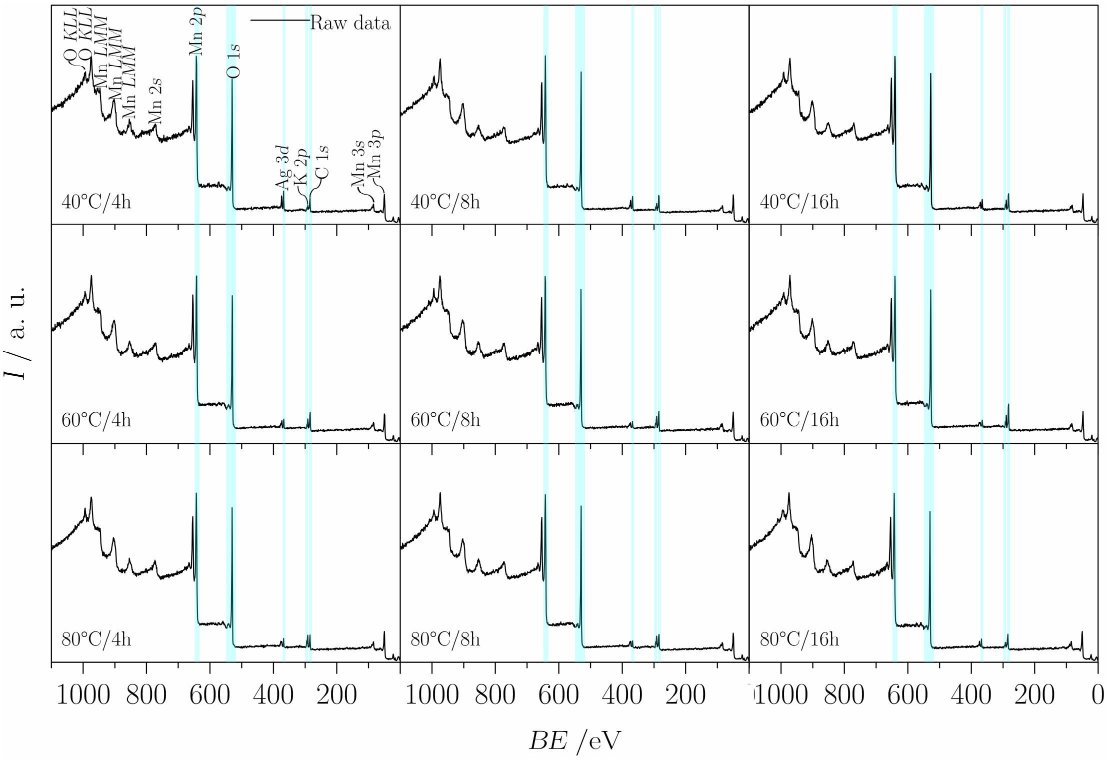

Figure S5. XP survey spectra of as-synthesized α-MnO$_2$. Cyan areas highlight features used for the determination of Mn, O, K, Ag and C elemental (surface) compositions. Prior to fitting, XPS raw data was charge corrected by Binding energy (*BE*) shifts of C-C/C-H partial emissions as obtained from resolved high-resolution C 1*s* core-level photoemission spectra and C-C/C-H line position of adventitious carbon located at 284.8 eV.[4,5] A Shirley-type background was applied to the charge corrected raw data.[6] Elemental compositions were calculated from relative areas of fitted high-resolution Mn 2$p_{3/2}$, O 1*s*, K 2*p*, Ag 3$d_{5/2}$ and C 1*s* core-level photoemission spectra using CasaXPS processing software.

Table S3. Summarized elemental (surface) compositions of Mn, O, K and Ag as calculated from relative areas of fitted high-resolution Mn 2$p_{3/2}$, O 1*s*, K 2*p* and Ag 3$d_{5/2}$ core-level photoemission spectra of as-synthesized α-MnO$_2$ using CasaXPS processing software (**Figure S5**). C as derived from high-resolution C 1*s* core-level photoemission spectra was deducted as it is regarded a surface contamination due to air exposure during sample preparation.[7]

α-MnO$_2$	Mn 2$p_{3/2}$	O 1*s*	K 2*p*	Ag 3$d_{5/2}$
T/*t*	at.-%	at.-%	at.-%	at.-%
40°C/4h	30.31	66.75	1.69	1.25
40°C/8h	30.81	65.56	2.68	0.95
40°C/16h	30.89	65.13	3.28	0.69
60°C/4h	30.10	65.81	3.50	0.59
60°C/8h	30.02	65.52	3.99	0.47
60°C/16h	30.08	65.21	4.34	0.37
80°C/4h	29.42	65.81	4.33	0.44
80°C/8h	30.21	64.75	4.57	0.45
80°C/16h	33.25	64.17	2.11	0.47

Section S3.3. Comparison of SEM-EDX and XPS elemental compositions

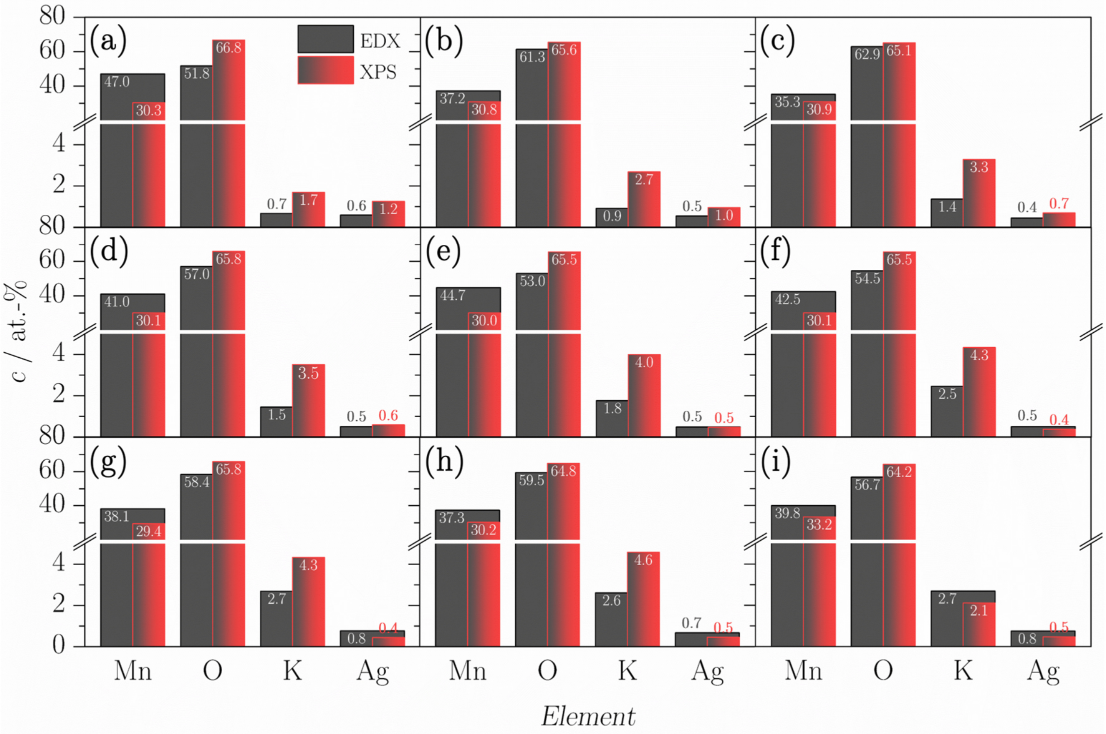

Figure S6. Comparison of SEM-EDX (gray columns) and XPS (gray-red graded columns) elemental compositions of as-synthesized α-MnO$_2$. (a) 40°C/4h, (b) 40°C/8h, (c) 40°C/16h, (d) 60°C/4h, (e) 60°C/8h, (f) 60°C/16h, (g) 80°C/4h, (h) 80°C/8h and (i) 80°C/16h. Columns representing the results from XPS are inserted into the gray columns of EDX in order to emphasize the different information depths of both techniques.

In general, both EDX and XPS agree well demonstrating as-synthesized α-MnO$_2$ to mainly consist of manganese (Mn) and oxygen (O), that can be certainly related to MnO$_2$. Moreover, minor portions of potassium (K) and silver (Ag) are detectable, though EDX and XPS yield slightly different results. This is due to different information depths of both techniques.[8] While the information depth of EDX, or the electron beam at 15 kV accelerating voltage, respectively, can be considered to range a few microns and thus probes almost complete (bulk) particles,[9] XPS gives the elemental composition to a depth of ~10 nm, that is the near surface, or outer region of the particles, respectively.[10,11] Accordingly, variations in elemental compositions can be used for elucidating inhomogeneities, e.g., concentration gradients across the particles. In the light of this, higher elemental contents derived by XPS are to be interpreted as a concentration gradient towards the outer of the particles, and, vice versa, an increasing concentration gradient towards the nucleus of the particles can be assumed when EDX detects higher elemental contents. On the other hand, equal contents indicate an elemental composition to be homogeneous over the cross-section of particles. Accordingly, two- to threefold higher K contents by XPS as compared to EDX, which are almost evenly increasing by increasing the temperature and dwell time of the synthesis, are representative for an increasing concentration gradient of K towards the outer of the particles. However, except for α-MnO_2 sea-urchins synthesized at 80°C/16h, where a higher K content by EDX denotes a concentration gradient towards the nucleus of the particles. Meanwhile, a comparison of Ag contents demonstrates concentrations gradients towards the surface, the core, as well as a homogeneous distribution for α-MnO_2 synthesized at ≤60°C/4h, ≥60°C/60h and 60°C/8h, respectively. Interestingly, the Ag concentration gradient is reversing at synthesis conditions giving rise to the spike shell leading to the assumption that the sea-urchin-like structure is preferentially occupied during a depletion, or even in absence of Ag, respectively.

Section S4. Resolved high-resolution C 1*s* core-level photoemission spectra of as-synthesized *α*-MnO₂ and reference Mn oxides

Section S4.1. As-synthesized *α*-MnO₂

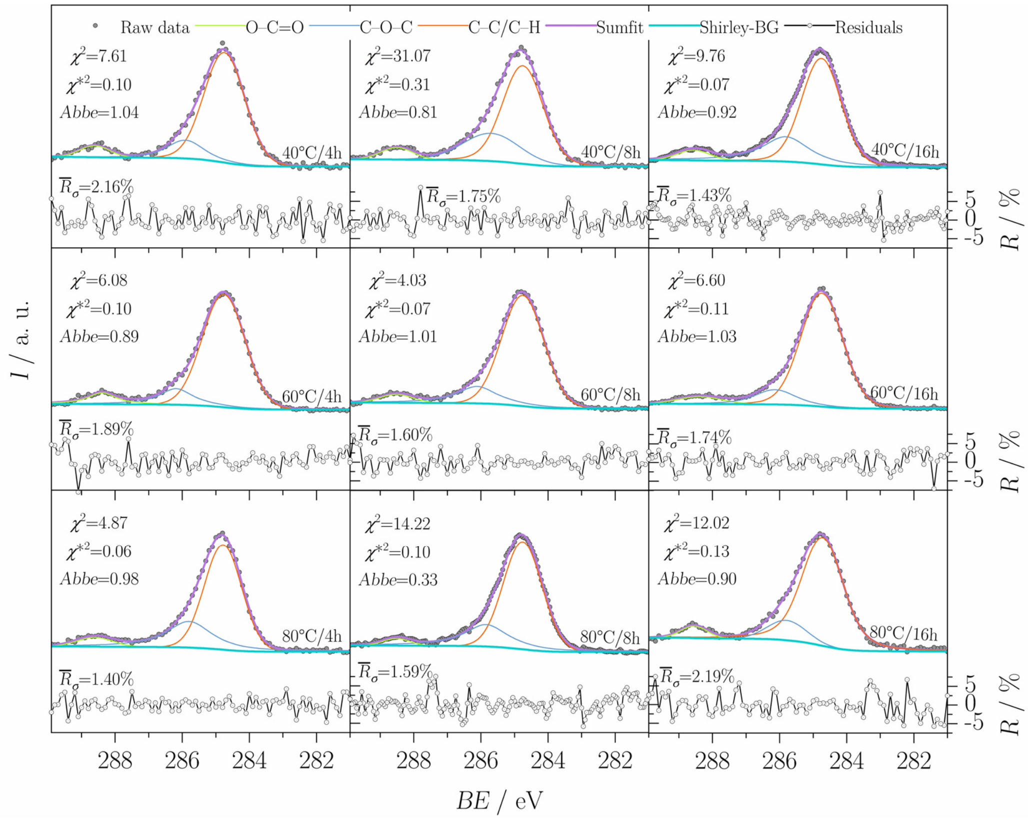

Figure S7. Resolved high-resolution C 1*s* core-level photoemission spectra of as-synthesized *α*-MnO₂ including percentage residuals and goodness of fit parameters. Prior to fitting a Shirley-type background was applied to the raw data.[6] C 1*s* core-level photoemission spectra were resolved by means of three components, i.e., O-C=O, C-O-C and C-C/C-H partial emissions,[12–14] respectively, using a total of three Voigt line profiles with *BE* positions, Lorentz-Gauss mixing parameters (*L*/*G* ratios) and full width at half maxima (*FWHM*) as suggested by Fityk evaluation software. The shift in binding energies of C-C/C-H partial emissions as obtained from resolved high-resolution C 1*s* core-level photoemission spectra and C-C/C-H component of adventitious carbon located at 284.8 eV were determined,[4] subsequently, charge correction was carried out by rigidly applying the same *BE* shift to all signals of the respective sample.[5]. Percentage residuals (*R*), its mean absolute deviation ($\overline{R}_\sigma$), chi-squared (χ^2), reduced chi-squared (χ^{*2}), and *Abbe* criteria are ranging from ±5% to ±7.5%, 1.40-2.19%, 7.61-31.07, 0.06-0.31 and 0.81-1.04, respectively, attributing suitable fits. Despite attempts to improve the fit, *Abbe* of *α*-MnO₂ synthesized at 80°C/8h is limited to a mere 0.33.

Table S4. Summarized *BE* positions of O-C=O ($BE_{\text{O-C=O}}$), C-O-C ($BE_{\text{C-O-C}}$) and C-C/C-H ($BE_{\text{C-C/C-H}}$) components as obtained from resolved high-resolution C 1*s* core-level photoemission spectra of as-synthesized α-MnO_2 (**Figure S7**). The values are derived from charge corrected signals.

α-MnO_2	$BE_{\text{O-C=O}}$	$BE_{\text{C-O-C}}$	$BE_{\text{C-C/C-H}}$[a]
T/*t*	eV	eV	eV
40°C/4h	288.61	285.91	284.80
40°C/8h	288.51	285.69	284.80
40°C/16h	288.56	285.81	284.80
60°C/4h	288.39	286.18	284.80
60°C/8h	288.51	286.11	284.80
60°C/16h	288.38	286.14	284.80
80°C/4h	288.60	285.80	284.80
80°C/8h	287.92	285.74	284.80
80°C/16h	288.55	285.79	284.80

[a] $BE_{\text{C-C/C-H}}$=284.8 eV=*const.* due to charge correction of C-C/C-H partial emissions as obtained from resolved high-resolution C 1*s* core-level photoemission spectra and C-C/C-H component of adventitious carbon located at 284.8 eV.

Section S4.2. Reference Mn oxides

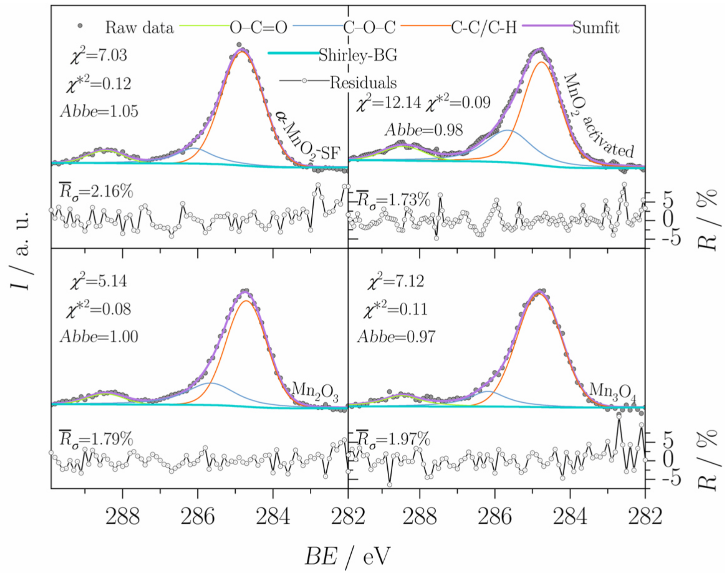

Figure S8: Resolved high-resolution C 1*s* core-level photoemission spectra of reference Mn oxides including percentage residuals and goodness of fit parameters. Prior to fitting a Shirley-type background was applied to the raw data.[6] C 1*s* core-level photoemission spectra were resolved by means of three components, i.e., O-C=O, C-O-C and C-C/C-H partial emissions,[12–14] respectively, using a total of three Voigt line profiles with *BE* positions, *L/G* ratios and *FWHM* as suggested by Fityk evaluation software. The shift in binding energies of C-C/C-H partial emissions as obtained from resolved high-resolution C 1*s* core-level photoemission spectra and C-C/C-H component of adventitious carbon located at 284.8 eV were determined,[4] subsequently, charge correction was carried out by rigidly applying the same *BE* shift to all signals of the respective sample.[5] R, $\overline{R}_{\sigma}$, χ^2, χ^{*2} and *Abbe* criteria are ranging from ±5% to ±7.5%, 1.73-2.16%, 5.14-12.14, 0.08-0.12 and 0.97-1.05, respectively, attributing sufficiently accurate fits.

Table S5. Summarized *BE* positions of O-C=O ($BE_{\text{O-C=O}}$), C-O-C ($BE_{\text{C-O-C}}$) and C-C/C-H ($BE_{\text{C-C/C-H}}$) components as obtained from resolved high-resolution C 1*s* core-level photoemission spectra of reference Mn oxides (**Figure S8**). The values are derived from charge corrected signals.

Mn oxide	$BE_{\text{O-C=O}}$ / eV	$BE_{\text{C-O-C}}$ / eV	$BE_{\text{C-C/C-H}}{}^{a}$ / eV
α-MnO_2-SF	288.45	286.09	284.80
MnO_2 activated	288.43	285.64	284.80
Mn_2O_3	288.46	285.65	284.80
Mn_3O_4	288.47	286.18	284.08

[a] $BE_{\text{C-C/C-H}}$=284.8 eV=*const.* due to charge correction of C-C/C-H partial emissions as obtained from resolved high-resolution C 1*s* core-level photoemission spectra and C-C/C-H component of adventitious carbon located at 284.8 eV

Section S5. Resolved high-resolution Mn $2p_{1/2}$ core-level photoemission spectra of as-synthesized α-MnO_2 and reference Mn oxides

Section S5.1. As-synthesized α-MnO_2

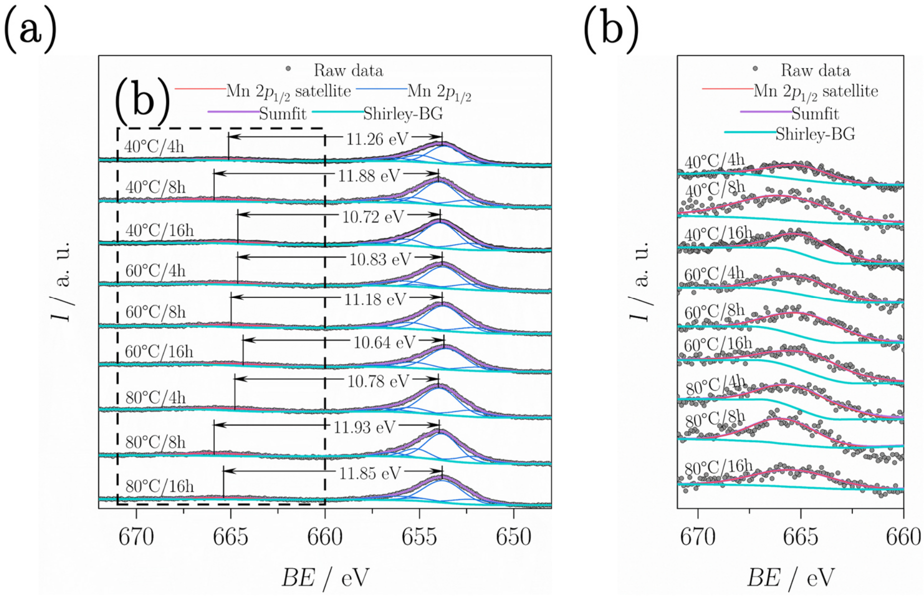

Figure S9. Resolved high-resolution Mn $2p_{1/2}$ core-level photoemission spectra of as-synthesized α-MnO_2. (a) Full Mn $2p_{1/2}$ regions highlighting the Mn $2p_{1/2}$ main peaks and (b) magnified Mn $2p_{1/2}$ charge-transfer satellites. Fitting was carried out without further constrains, i.e., using *BE* positions, *L*/*G* ratios (not included) and *FWHM* (not included) as suggested by Fityk evaluation software. Mn $2p_{1/2}$ main peaks were fitted by means of three Voigt line profiles, though charge-transfer satellites could be resolved sufficiently accurate using one Voigt line profile. Energy splittings ($\Delta E_{\mathrm{Mn}\ 2p_{1/2}}$) were determined by the relative distance of Mn $2p_{1/2}$ main peaks and charge-transfer satellites based on sumfits.[15,16] Percentage residuals and goodness of fit parameters are summarized in **Figure S19** and **Table S17**.

Table S6. Summarized *BE* positions of Mn 2$p_{1/2}$ main peaks ($BE_{\mathrm{Mn}\ 2p_{1/2}}$) and charge-transfer satellites ($BE_{\mathrm{satellite}}$) as obtained from sumfits of high-resolution Mn 2$p_{1/2}$ core-level photoemission spectra of as-synthesized α-MnO$_2$ (**Figure S9**). Energy splittings ($\Delta E_{\mathrm{Mn}\ 2p_{1/2}}$) were determined by the relative distance of Mn 2$p_{1/2}$ main peaks and charge-transfer satellites, i.e., based on $\Delta E_{\mathrm{Mn}\ 2p_{1/2}}=BE_{\mathrm{satellite}}-BE_{\mathrm{Mn}\ 2p_{1/2}}$.[15,16]

α-MnO$_2$ *T/t*	$BE_{\mathrm{Mn}\ 2p_{1/2}}$ eV	$BE_{\mathrm{satellite}}$ eV	$\Delta E_{\mathrm{Mn}\ 2p_{1/2}}$ [a] eV
40°C/4h	653.85	665.11	11.26
40°C/8h	654	665.88	11.88
40°C/16h	653.9	664.62	10.72
60°C/4h	653.8	664.63	10.83
60°C/8h	653.8	664.98	11.18
60°C/16h	653.7	664.34	10.64
80°C/4h	654	664.78	10.78
80°C/8h	653.95	665.88	11.93
80°C/16h	653.8	665.38	11.58

[a] $\Delta E_{\mathrm{Mn}\ 2p_{1/2}}=BE_{\mathrm{satellite}}-BE_{\mathrm{Mn}\ 2p_{1/2}}$

Section S5.2. Reference Mn oxides

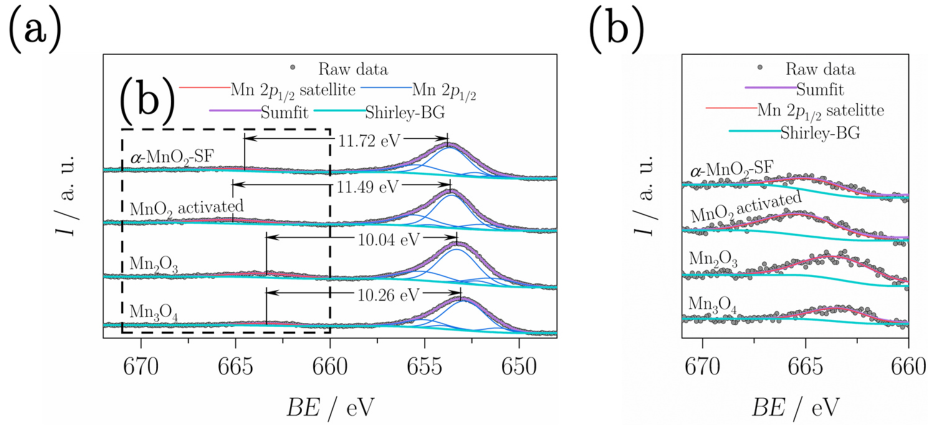

Figure S10. Resolved high-resolution Mn $2p_{1/2}$ core-level photoemission spectra of reference Mn oxides. (a) Full Mn $2p_{1/2}$ regions highlighting the Mn $2p_{1/2}$ main peaks and (b) magnified Mn $2p_{1/2}$ charge-transfer satellites. Fitting was carried out without further restrains, i.e., using *BE* positions, *L/G* ratios (not included) and *FWHM* (not included) as suggested by Fityk evaluation software. Mn $2p_{1/2}$ main peaks were fitted by means of three Voigt line profiles, though charge-transfer satellites could be resolved sufficiently accurate using one Voigt line profile. Energy splittings ($\Delta E_{\mathrm{Mn}\ 2p_{1/2}}$) were determined by the relative distance of Mn $2p_{1/2}$ main peaks and charge-transfer satellites based on sumfits.[15,16] Percentage residuals and goodness of fit parameters are summarized in **Figure S20** and **Table S18**.

Table S7. Summarized *BE* positions of Mn $2p_{1/2}$ main peaks ($BE_{\mathrm{Mn}\ 2p_{1/2}}$) and charge-transfer satellites ($BE_{\mathrm{satellite}}$) as obtained from sumfits of high-resolution Mn $2p_{1/2}$ core-level photoemission spectra of reference Mn oxides (**Figure S10**). Energy splittings ($\Delta E_{\mathrm{Mn}\ 2p_{1/2}}$) were determined by the relative distance of Mn $2p_{1/2}$ main peaks and charge-transfer satellites, i.e., based on $\Delta E_{\mathrm{Mn}\ 2p_{1/2}}=BE_{\mathrm{satellite}}-BE_{\mathrm{Mn}\ 2p_{1/2}}$.[15,16]

Mn oxide	$BE_{\mathrm{Mn}\ 2p_{1/2}}$ / eV	$BE_{\mathrm{satellite}}$ / eV	$\Delta E_{\mathrm{Mn}\ 2p_{1/2}}$ [a] / eV
α-MnO$_2$-SF	653.8	664.52	10.72
MnO$_2$ activated	653.65	665.14	11.49
Mn$_2$O$_3$	653.3	663.34	10.04
Mn$_3$O$_4$	653.1	663.36	10.26

[a] $\Delta E_{\mathrm{Mn}\ 2p_{1/2}}=BE_{\mathrm{satellite}}-BE_{\mathrm{Mn}\ 2p_{1/2}}$

Section S6. Resolved high-resolution O 1*s* core-level photoemission spectra of as-synthesized *α*-MnO_2 and reference Mn oxides

Section S6.1. As-synthesized *α*-MnO_2

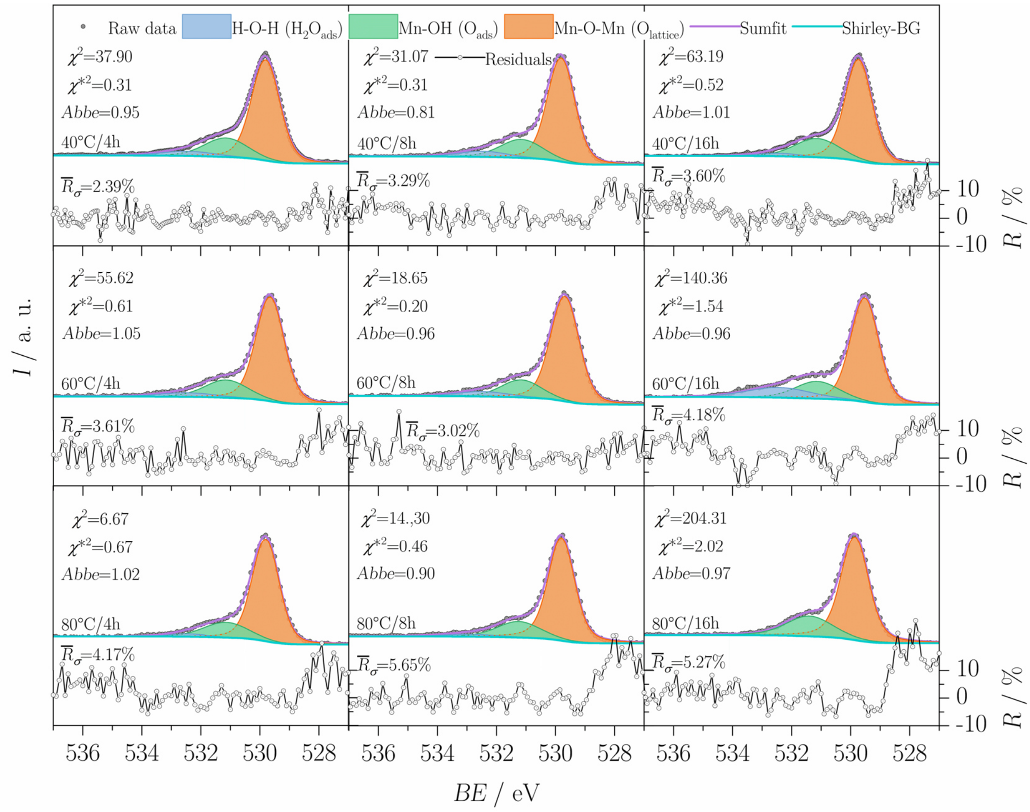

Figure S11. Resolved high-resolution O 1*s* core-level photoemission spectra of as-synthesized *α*-MnO_2 including percentage residuals and goodness of fit parameters. O 1*s* core-level photoemission spectra were resolved by means of a H-O-H, Mn-OH and Mn-O-Mn component attributed to carbon-oxygen species, or adsorbed molecular water (denoted H_2O_{ads}), surface adsorbed oxygen with low coordination (O^{2-} or O^{-}), i.e., surface OH^{-}-like groups, or defective oxygen (denoted O_{ads}), and lattice oxygen (denoted $O_{lattice}$), respectively.[17–19] Thus, a total of three Voigt line profiles with *L*/*G*=0.25 and *BE* positions of H-O-H (H_2O_{ads}) and Mn-OH (O_{ads}) being constrained were used for the mathematical deconvolution. In contrary, suitable *BE* positions for fitting Mn-O-Mn ($O_{lattice}$) components as well as *FWHM* (not included) were exploited as suggested by Fityk evaluation software. No adsorbed molecular water (H_2O_{ads}) could be found for *α*-MnO_2 synthesized at 80°C/16h. *R*, $\overline{R}_\sigma$, χ^2, χ^{*2} and *Abbe* are ranging from ±7.5 to ±10%, 2.39-5.65%, 6.67-204, 0.21-2.20 and 0.81-1.05, respectively, attributing accurate fits.

Table S8. Summarized *BE* positions and individual mole fractions of H-O-H ($BE_{H_2O_{ads}}$, $X_{H_2O_{ads}}$), Mn-OH ($BE_{O_{ads}}$, $X_{O_{ads}}$) and Mn-O-Mn ($BE_{O_{lattice}}$, $X_{O_{lattice}}$) components as obtained from the relative areas of Voigt line profiles exploited in the mathematical deconvolution of high-resolution O 1*s* core-level photoemission spectra of as-synthesized α-MnO$_2$ (**Figure S11**). While $BE_{H_2O_{ads}}$=532.45 eV, $BE_{O_{ads}}$=531.14 eV and *L*/*G*=0.25 were constrained, *BE* positions for fitting O$_{lattice}$ components ($BE_{O_{lattice}}$) as well as and *FWHM* (not included) were used as suggested by Fityk evaluation software. However, suitable $BE_{O_{lattice}}$ are ranging from 529.53-529.86 eV. No adsorbed molecular water (H$_2$O$_{ads}$) could be found for α-MnO$_2$ synthesized at 80°C/16h.

α-MnO$_2$ *T*/*t*	$BE_{H_2O_{ads}}$ eV	$X_{H_2O_{ads}}$ mol-%	$BE_{O_{ads}}$ eV	$X_{O_{ads}}$ mol-%	$BE_{O_{lattice}}$ eV	$X_{O_{lattice}}$ mol-%
40°C/4h	532.45	6.31	531.14	20.81	529.80	72.63
40°C/8h	532.45	6.87	531.14	19.94	529.80	73.18
40°C/16h	532.45	3.28	531.14	22.46	529.74	74.26
60°C/4h	532.45	5.69	531.14	19.23	529.66	75.08
60°C/8h	532.45	6.36	531.14	17.63	529.67	76.01
60°C/16h	532.45	14.89	531.14	17.30	529.53	67.80
80°C/4h	532.45	3.01	531.14	19.10	529.80	77.89
80°C/8h	532.45	3.61	531.14	19.43	529.80	76.96
80°C/16h	—	—	531.14	24.56	529.86	75.44

Section S6.2. Reference Mn oxides

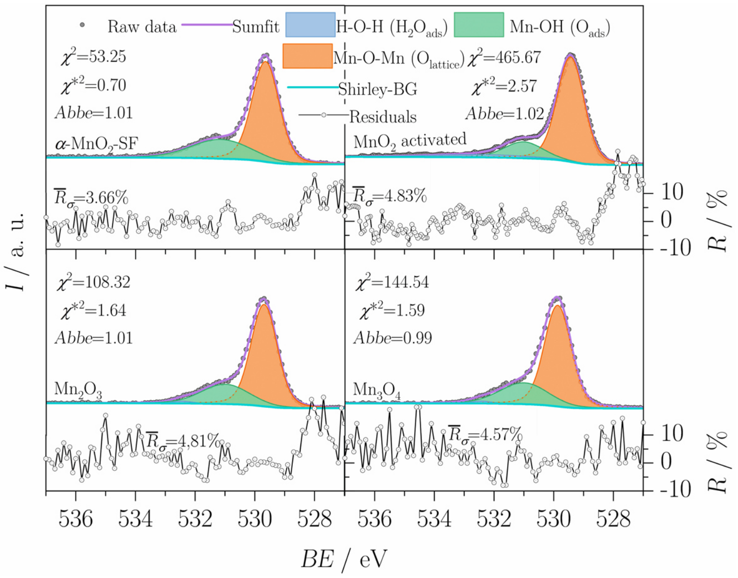

Figure S12. Resolved high-resolution O 1*s* core-level photoemission spectra of reference Mn oxides including percentage residuals and goodness of fit parameters. O 1*s* core-level photoemission spectra were resolved by means of a H-O-H, Mn-OH and Mn-O-Mn component attributed to carbon-oxygen species, or adsorbed molecular water (denoted H_2O_{ads}), surface adsorbed oxygen with low coordination (O^{2-} or O^-), i.e., surface OH^--like groups, or defective oxygen (denoted O_{ads}), and lattice oxygen (denoted $O_{lattice}$), respectively.[17–19] Thus, a total of three Voigt line profiles with *BE* positions of H-O-H (H_2O_{ads}) and Mn-OH (O_{ads}) components as well as *L*/*G*=0.25 being constrained were used for the mathematical deconvolution. In contrary, suitable *BE* positions for fitting Mn-O-Mn ($O_{lattice}$) components as well as *FWHM* (not included) were exploited as suggested by Fityk evaluation software. No adsorbed molecular water (H_2O_{ads}) could be found for α-MnO_2-SF. R, $\overline{R}_\sigma$, χ^2, χ^{*2} and *Abbe* are ranging from ±7.5% to ±10%, 3.66-4.83%, 53.25-465.67, 0.70-2.57 and 0.99-1.02, respectively, indicating sufficiently accurate fits.

Table S9. Summarized *BE* positions and individual mole fractions of H-O-H ($BE_{H_2O_{ads}}$, $X_{H_2O_{ads}}$), Mn-OH ($BE_{O_{ads}}$, $X_{O_{ads}}$) and Mn-O-Mn ($BE_{O_{lattice}}$, $X_{O_{lattice}}$) components as obtained from the relative areas of Voigt line profiles exploited in the mathematical deconvolution of high-resolution O 1*s* core-level photoemission spectra of reference Mn oxides (**Figure S12**). While $BE_{H_2O_{ads}}$=532.45 eV, $BE_{O_{ads}}$=531.14 eV and *L*/*G*=0.25 were constrained, *BE* positions for fitting $O_{lattice}$ components ($BE_{O_{lattice}}$) as well as *FWHM* (not included) were used as suggested by Fityk evaluation software. However, suitable $BE_{O_{lattice}}$ are in the range of 529.43-529.87 eV. No adsorbed molecular water (H_2O_{ads}) could be found for α-MnO_2-SF.

Mn oxide	$BE_{H_2O_{ads}}$ / eV	$X_{H_2O_{ads}}$ / mol-%	$BE_{O_{ads}}$ / eV	$X_{O_{ads}}$ / mol-%	$BE_{O_{lattice}}$ / eV	$X_{O_{lattice}}$ / mol-%
α-MnO_2-SF	—	—	531.14	29.53	529.64	70.47
MnO_2 activated	532.45	7.81	531.01	16.73	529.43	75.46
Mn_2O_3	532.45	1.25	531.01	25.73	529.70	73.02
Mn_3O_4	532.45	1.29	531.01	27.19	529.87	71.52

Section S7. Resolved high-resolution Mn 3*s* core-level photoemission spectra of as-synthesized *α*-MnO_2 and reference Mn oxides

Section S7.1. As-synthesized *α*-MnO_2

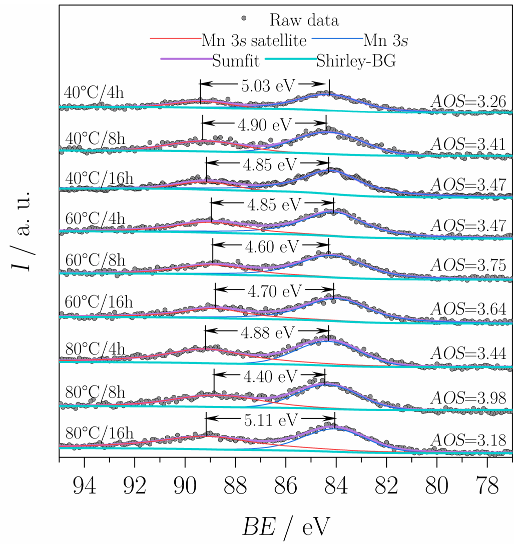

Figure S13. Resolved high-resolution Mn 3*s* core-level photoemission spectra of as-synthesized *α*-MnO_2. Mn 3s photoemission spectra were resolve by means of a Voigt line profile each for the main peak and satellite using *BE* positions, *L*/*G* ratios (not included) and *FWHM* (not included) as suggested by Fityk evaluation software. Energy splittings ($\Delta E_{\text{Mn }3s}$) are determined by maxima of single Voigt line profiles. Average oxidation states (*AOS*) are calculated based on *AOS*=8.95-1.13 $\Delta E_{\text{Mn }3s}$.[20–26] Percentage residuals and goodness of fit parameters are summarized in **Figure S21** and **Table S19**.

Table S10. Summarized *BE* positions of Mn 3*s* main peaks ($BE_{\text{Mn }3s}$) and satellites ($BE_{\text{satellite}}$) as obtained from single Voigt line profiles of resolved high-resolution Mn 3s core-level photoemission spectra of as-synthesized α-MnO_2 (**Figure S13**). Energy splittings ($\Delta E_{\text{Mn }3s}$) are determined based on $\Delta E_{\text{Mn }3s}=BE_{\text{satellite}}-BE_{\text{Mn }3s}$. Average oxidation states (*AOS*) are calculated by $AOS=8.95-1.13\ \Delta E_{\text{Mn }3s}$.[20–26]

α-MnO_2 / T/t	$BE_{\text{Mn }3s}$ / eV	$BE_{\text{satellite}}$ / eV	$\Delta E_{\text{Mn }3s}$[a] / eV	AOS[b]
40°C/4h	84.27	89.30	5.03	3.26
40°C/8h	84.40	89.30	4.90	3.41
40°C/16h	84.30	89.15	4.85	3.47
60°C/4h	84.11	88.96	4.85	3.47
60°C/8h	83.30	88.90	4.60	3.75
60°C/16h	84.10	88.80	4.70	3.64
80°C/4h	84.31	89.18	4.88	3.44
80°C/8h	84.45	88.85	4.40	3.98
80°C/16h	84.05	89.16	5.11	3.18

[a] $\Delta E_{\text{Mn }3s}=BE_{\text{satellite}}-BE_{\text{Mn }3s}$

[b] $AOS=8.95-1.13\ \Delta E_{\text{Mn }3s}$

Section S7.2. Reference Mn oxides

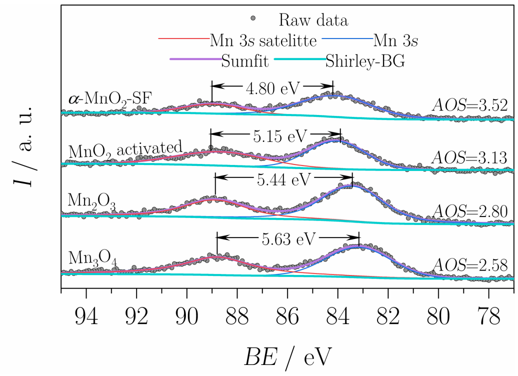

Figure S14. Resolved high-resolution Mn 3*s* core-level photoemission spectra of reference Mn oxides. Mn 3s photoemission spectra were resolve by means of a Voigt line profile each for the main peak and satellite using *BE* positions, *L*/*G* ratios (not included) and *FWHM* (not included) as suggested by Fityk evaluation software. Energy splittings ($\Delta E_{\mathrm{Mn}\ 3s}$) are determined by maxima of single Voigt line profiles. Average oxidation states (*AOS*) are calculated based on $AOS=8.95-1.13\ \Delta E_{\mathrm{Mn}\ 3s}$.[20–26] Percentage residuals and goodness of fit parameters are summarized in **Figure S22** and **Table S20**.

Table S11. Summarized *BE* positions of Mn 3*s* main peaks ($BE_{\mathrm{Mn}\ 3s}$) and satellites ($BE_{\mathrm{satellite}}$) as obtained from single Voigt line profiles of resolved high-resolution Mn 3s core-level photoemission spectra of reference Mn oxides (**Figure S14**). Energy splittings ($\Delta E_{\mathrm{Mn}\ 3s}$) are determined based on $\Delta E_{\mathrm{Mn}\ 3s}=BE_{\mathrm{satellite}}-BE_{\mathrm{Mn}\ 3s}$. Average oxidation states (*AOS*) are calculated by $AOS=8.95-1.13\ \Delta E_{\mathrm{Mn}\ 3s}$.[20–26]

Mn oxide	$BE_{\mathrm{Mn}\ 3s}$ / eV	$BE_{\mathrm{satellite}}$ / eV	$\Delta E_{\mathrm{Mn}\ 3s}$[a] / eV	*AOS*[b]
α-MnO_2-SF	84.20	89.00	4.80	3.52
MnO_2 activated	83.90	89.05	5.15	3.13
Mn_2O_3	83.42	88.87	5.44	2.80
Mn_3O_4	83.16	88.80	5.63	2.58

[a] $\Delta E_{\mathrm{Mn}\ 3s}=BE_{\mathrm{satellite}}-BE_{\mathrm{Mn}\ 3s}$

[b] $AOS=8.95-1.13\ \Delta E_{\mathrm{Mn}\ 3s}$

Section S8. Constrained binding energy positions of Voigt line profiles used for the mathematical deconvolution of high-resolution Mn 2$p_{3/2}$ core-level photoemission spectra

Table S12. Constrained *BE* positions of Voigt line profiles used for the mathematical deconvolution of high-resolution Mn 2$p_{3/2}$ core-level photoemission spectra. (a) Mn^{4+}, (b) Mn^{3+} and (c) Mn^{2+}.

(a)

$\frac{BE_1}{\mathrm{eV}}$	$\frac{\Delta BE_{1/2}}{\mathrm{eV}}$	$\frac{BE_2}{\mathrm{eV}}$	$\frac{\Delta BE_{2/3}}{\mathrm{eV}}$	$\frac{BE_3}{\mathrm{eV}}$	$\frac{\Delta BE_{3/4}}{\mathrm{eV}}$	$\frac{BE_4}{\mathrm{eV}}$	$\frac{\Delta BE_{4/5}}{\mathrm{eV}}$	$\frac{BE_5}{\mathrm{eV}}$	$\frac{\Delta BE_{5/6}}{\mathrm{eV}}$	$\frac{BE_6}{\mathrm{eV}}$
642.10	0.78	642.88	0.59	643.47	0.70	644.17	0.78	644.95	0.91	645.86

(b)

$\frac{BE_7}{\mathrm{eV}}$	$\frac{\Delta BE_{7/8}}{\mathrm{eV}}$	$\frac{BE_8}{\mathrm{eV}}$	$\frac{\Delta BE_{8/9}}{\mathrm{eV}}$	$\frac{BE_9}{\mathrm{eV}}$	$\frac{\Delta BE_{9/10}}{\mathrm{eV}}$	$\frac{BE_{10}}{\mathrm{eV}}$	$\frac{\Delta BE_{10/11}}{\mathrm{eV}}$	$\frac{BE_{11}}{\mathrm{eV}}$	$\frac{\Delta BE_{11/12}}{\mathrm{eV}}$	$\frac{BE_{12}}{\mathrm{eV}}$
640.85	0.79	641.64	0.68	642.32	0.76	643.08	0.82	643.9	0.84	644.74

(c)

$\frac{BE_{13}}{\mathrm{eV}}$	$\frac{\Delta BE_{12/14}}{\mathrm{eV}}$	$\frac{BE_{14}}{\mathrm{eV}}$	$\frac{\Delta BE_{14/15}}{\mathrm{eV}}$	$\frac{BE_{15}}{\mathrm{eV}}$	$\frac{\Delta BE_{15/16}}{\mathrm{eV}}$	$\frac{BE_{16}}{\mathrm{eV}}$	$\frac{\Delta BE_{16/17}}{\mathrm{eV}}$	$\frac{BE_{17}}{\mathrm{eV}}$	$\frac{\Delta BE_{17/18}}{\mathrm{eV}}$	$\frac{BE_{18}}{\mathrm{eV}}$
639.35	1.04	640.39	0.76	641.15	0.88	642.03	1.08	643.11	1.09	644.20

Section S9. Resolved high-resolution Mn 2*p*$_{3/2}$ core-level photoemission spectra of reference Mn oxides

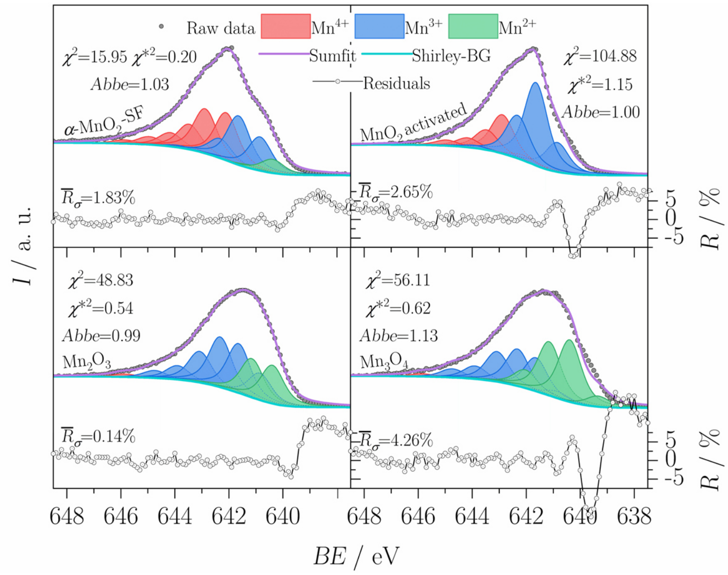

Figure S15. Resolved high-resolution Mn 2*p*$_{3/2}$ core-level photoemission spectra of reference Mn oxides including percentage residuals and goodness of fit parameters. Fitting was carried out by considering up to six Voigt line profiles for the Mn^{4+}, Mn^{3+} and Mn^{2+} component,[27] respectively, with *BE* positions (**Table S16**), *L*/*G*=0.5 and *FWHM*=1.02 being constrained. *R*, $\overline{R}_\sigma$, χ^2, χ^{*2} and *Abbe* are ranging from ±2.5% to ±7.5%, 0.14-4.26, 15.95-104.88, 0.20-1.15 and 0.99-1.15 indicating the fits are suitable as well as sufficiently accurate accomplished.

Section S10. Individual mole fractions of Mn^{4+}, Mn^{3+} and Mn^{2+} components as obtained from the mathematical deconvolution of high-resolution Mn $2p_{3/2}$ core-level photoemission spectra of as-synthesized α-MnO_2 and reference Mn oxides

Section S10.1. As-synthesized α-MnO_2

Table S13. Summarized individual mole fractions of Mn^{4+} ($X_{Mn^{4+}}$), Mn^{3+} ($X_{Mn^{3+}}$) and Mn^{2+} ($X_{Mn^{2+}}$) components of as-synthesized α-MnO_2. Mole fractions are equivalent to the relative areas of Voigt line profiles used for the mathematical deconvolution of high-resolution Mn $2p_{3/2}$ core-level photoemission spectra.

$\frac{\alpha\text{-MnO}_2}{T/t}$	$\frac{X_{Mn^{4+}}}{\text{mol-\%}}$							$\frac{X_{Mn^{3+}}}{\text{mol-\%}}$							$\frac{X_{Mn^{2+}}}{\text{mol-\%}}$						
	BE_1	*BE_2*	*BE_3*	*BE_4*	*BE_5*	*BE_6*	$\sum X_{Mn^{4+}}$	*BE_7*	*BE_8*	*BE_9*	*BE_{10}*	*BE_{11}*	*BE_{12}*	$\sum X_{Mn^{3+}}$	*BE_{13}*	*BE_{14}*	*BE_{15}*	*BE_{16}*	*BE_{17}*	*BE_{18}*	$\sum X_{Mn^{2+}}$
40°C/4h	14.29	14.56	9.10	3.78	2.64	1.70	46.07	12.57	17.59	14.39	3.80	4.00	1.58	53.93	—	—	—	—	—	—	—
40°C/8h	18.04	10.68	9.14	4.06	3.46	1.20	46.58	12.04	14.31	14.16	7.87	3.76	1.28	53.42	—	—	—	—	—	—	—
40°C/16h	21.18	16.41	10.03	5.14	2.12	1.58	56.46	13.94	15.72	8.45	2.36	1.93	1.14	43.54	—	—	—	—	—	—	—
60°C/4h	19.67	14.12	7.73	4.75	2.88	1.16	50.31	15.99	18.01	8.67	4.15	2.33	0.53	49.68	—	—	—	—	—	—	—
60°C/8h	22.29	18.91	9.58	3.92	1.71	1.65	58.06	12.19	17.97	4.98	—	2.32	2.11	39.57	—	—	—	—	2.38	—	2.38
60°C/16h	21.65	17.79	7.37	3.99	1.90	1.04	53.74	18.25	20.37	2.81	—	1.57	1.31	44.31	—	—	—	—	1.95	—	1.95
80°C/4h	21.29	12.62	9.34	4.89	2.40	1.79	52.33	10.84	12.19	11.75	6.69	3.18	1.53	46.18	—	—	—	1.50	—	—	1.50
80°C/8h	24.98	16.91	12.53	6.47	2.92	1.26	65.07	11.07	11.85	8.18	2.40	—	0.64	34.14	—	—	—	0.77	0.01	—	0.78
80°C/16h	11.26	12.39	7.42	2.13	2.18	1.87	37.25	17.74	18.37	15.17	4.49	5.21	1.75	62.73	—	—	—	—	—	—	—

Section S10.2. Reference Mn oxides

Table S14. Summarized individual mole fractions of Mn^{4+} ($X_{Mn^{4+}}$), Mn^{3+} ($X_{Mn^{3+}}$) and Mn^{2+} ($X_{Mn^{2+}}$) components of reference Mn oxides. Mole fractions are equivalent to the relative areas of Voigt line profiles used for the mathematical deconvolution of high-resolution Mn $2p_{3/2}$ core-level photoemission spectra.

Mn oxide	$\frac{X_{Mn^{4+}}}{\text{mol-\%}}$							$\frac{X_{Mn^{3+}}}{\text{mol-\%}}$							$\frac{X_{Mn^{2+}}}{\text{mol-\%}}$						
	BE_1	BE_2	BE_3	BE_4	BE_5	BE_6	$\sum X_{Mn^{4+}}$	BE_7	BE_8	BE_9	BE_{10}	BE_{11}	BE_{12}	$\sum X_{Mn^{3+}}$	BE_{13}	BE_{14}	BE_{15}	BE_{16}	BE_{17}	BE_{18}	$\sum X_{Mn^{2+}}$
α-MnO_2-SF	17.97	16.82	9.51	5.22	3.04	1.42	53.98	12.74	18.54	7.35	—	0.81	0.08	39.52	—	5.18	1.31	—	—	—	6.49
MnO_2 activated	2.21	16.28	8.40	3.97	2.41	0.12	33.39	12.32	34.81	18.07	—	1.19	0.22	66.61	—	—	—	—	—	—	—
Mn_2O_3	—	—	—	—	0.08	1.15	1.23	10.23	18.75	19.15	11.87	5.34	2.86	68.20	—	14.59	14.76	1.20	—	—	30.55
Mn_3O_4	—	—	—	—	—	1.04	1.04	2.48	12.07	13.34	10.89	4.72	3.14	46.64	3.88	22.41	19.44	6.58	—	—	52.31

Section S11. Further XPS analysis of as-synthesized α-MnO$_2$ and reference Mn oxides

Section S11.1. As-synthesized α-MnO$_2$

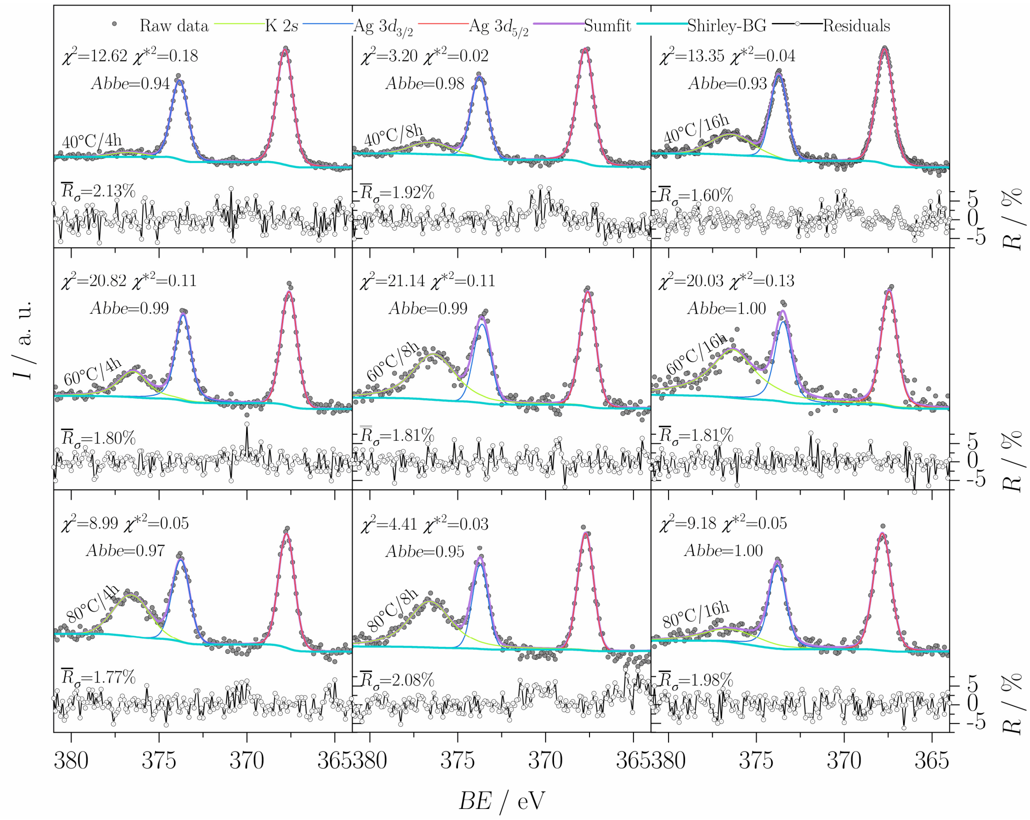

Figure S16. Resolved high-resolution K 2*s*, Ag 3$d_{3/2}$ and Ag 3$d_{5/2}$ core-level photoemission spectra of as-synthesized α-MnO$_2$ including percentage residuals and goodness of fit parameters. K 2*s*, Ag 3$d_{3/2}$ and Ag 3$d_{5/2}$ photoemission spectra were resolved by means one Voigt line profile each using *BE* positions, *L*/*G* ratios (not included) and *FWHM* (not included) as suggested by Fityk evaluation software. R, $\overline{R}_{\sigma}$, χ^2, χ^{*2} and *Abbe* are ranging from ±5% to ±7.5%. 1.60-2.13%, 3.20-21.14, 0.02-0.18 and 0.93-1.00, respectively, indicating sufficiently accurate fits.

Table S15. Summarized *BE* positions of K 2*s* ($BE_{\text{K 2s}}$), Ag 3*d*$_{3/2}$ ($BE_{\text{Ag }3d_{3/2}}$) and Ag 3*d*$_{5/2}$ ($BE_{\text{Ag }3d_{5/2}}$) components as obtained from single Voigt line profiles (**Figure S16**). *BE* positions, *L*/*G* ratios (not included) and *FWHM* (not included) were used as suggested by Fityk evaluation software. However, suitable *BE* positions for K 2*s*, Ag 3*d*$_{3/2}$ and Ag 3*d*$_{5/2}$ components are ranging from 376.33-376.84 eV, 373.48-373.83 eV and 367.44-367.84 eV, respectively.

α-MnO$_2$	$BE_{\text{K }2s}$	$BE_{\text{Ag }3d_{3/2}}$	$BE_{\text{Ag }3d_{5/2}}$
T/*t*	eV	eV	eV
40°C/4h	376.84	373.83	367.84
40°C/8h	376.58	373.76	367.74
40°C/16h	376.43	373.71	357.70
60°C/4h	376.48	373.63	367.60
60°C/8h	376.36	373.61	367.60
60°C/16h	376.33	373.48	367.44
80°C/4h	376.57	373.75	367.74
80°C/8h	376.58	373.76	367.74
80°C/16h	376.41	373.80	367.83

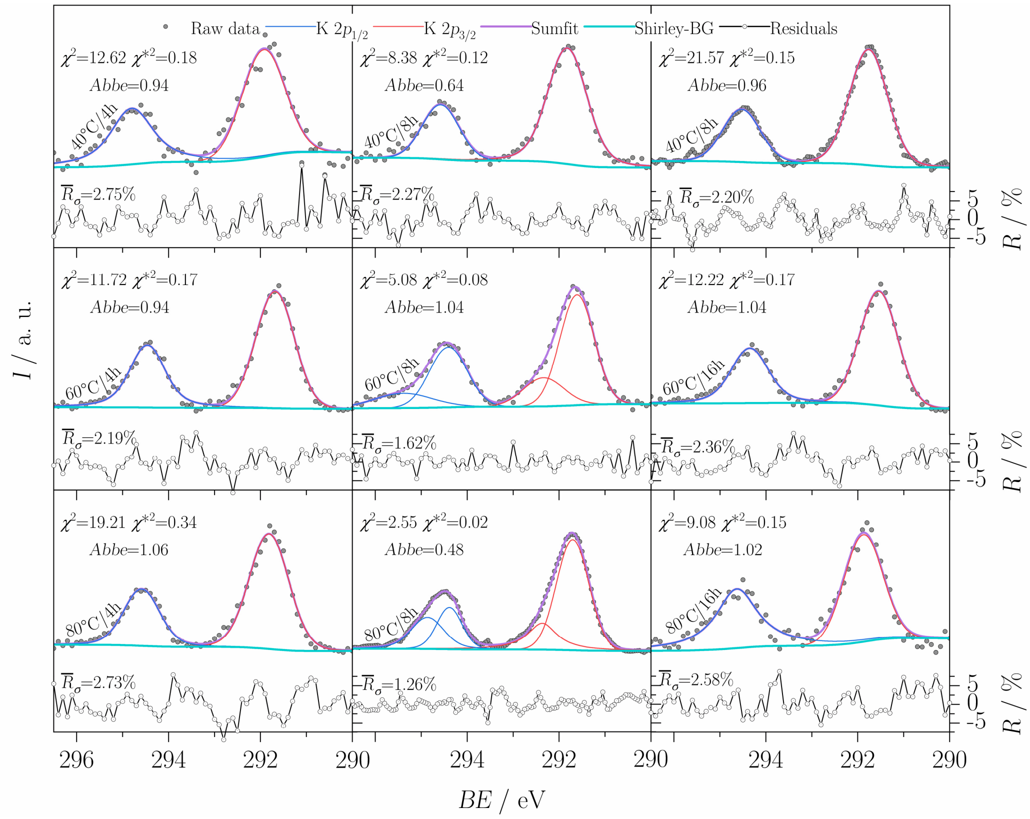

Figure S17. Resolved high-resolution K $2p_{1/2}$ and K $2p_{3/2}$ core-level photoemission spectra of as-synthesized α-MnO_2 including percentage residuals and goodness of fit parameters. For α-MnO_2 synthesized at 60°C/8h and 80°C/8h a asymmetric tail towards higher binding energies could be identified within the K $2p_{1/2}$ and K $2p_{3/2}$ peaks, hence they were resolved by two Voigt line profiles each in order to obtain an accurate fit. Other as-synthesized α-MnO_2 could be resolved by a total of two Voigt line profiles. *BE* positions, *L*/*G* ratios (not included) and *FWHM* (not included) were used as suggested by Fityk evaluation software. R, $\overline{R}_\sigma$, χ^2, χ^{*2} and *Abbe* are ranging from ±5% to ±7.5%, 1.26-3.27%, 2.55-21.57, 0.02-0.34 and 0.48-1.06, respectively, indicating sufficiently accurate fits.

Table S16. Summarized *BE* positions of K 2*p*$_{1/2}$ ($BE_{\mathrm{K}\ 2p_{1/2}}$) and K 2*p*$_{3/2}$ ($BE_{\mathrm{K}\ 2p_{3/2}}$) components as obtained from maxima of single Voigt line profiles, or sumfits, respectively (**Figure S17**). *BE* positions, *L/G* ratios (not included) and *FWHM* (not included) were used as suggested by Fityk evaluation software. However, suitable *BE* positions of K 2*p*$_{1/2}$ and K 2*p*$_{3/2}$ components are in the range of 294.35-294.80 eV and 291.54-291.93 eV, respectively.

$\frac{\alpha\text{-MnO}_2}{T/t}$	$\frac{BE_{\mathrm{K}\ 2p_{1/2}}}{\mathrm{eV}}$	$\frac{BE_{\mathrm{K}\ 2p_{3/2}}}{\mathrm{eV}}$
40°C/4h	294.80	291.93
40°C/8h	294.58	291.82
40°C/16h	294.53	291.77
60°C/4h	294.46	291.68
60°C/8h	294.40	291.60
60°C/16h	294.35	291.54
80°C/4h	294.59	291.81
80°C/8h	294.50	291.70
80°C/16h	294.63	291.88

Section S11.2. Reference Mn oxides

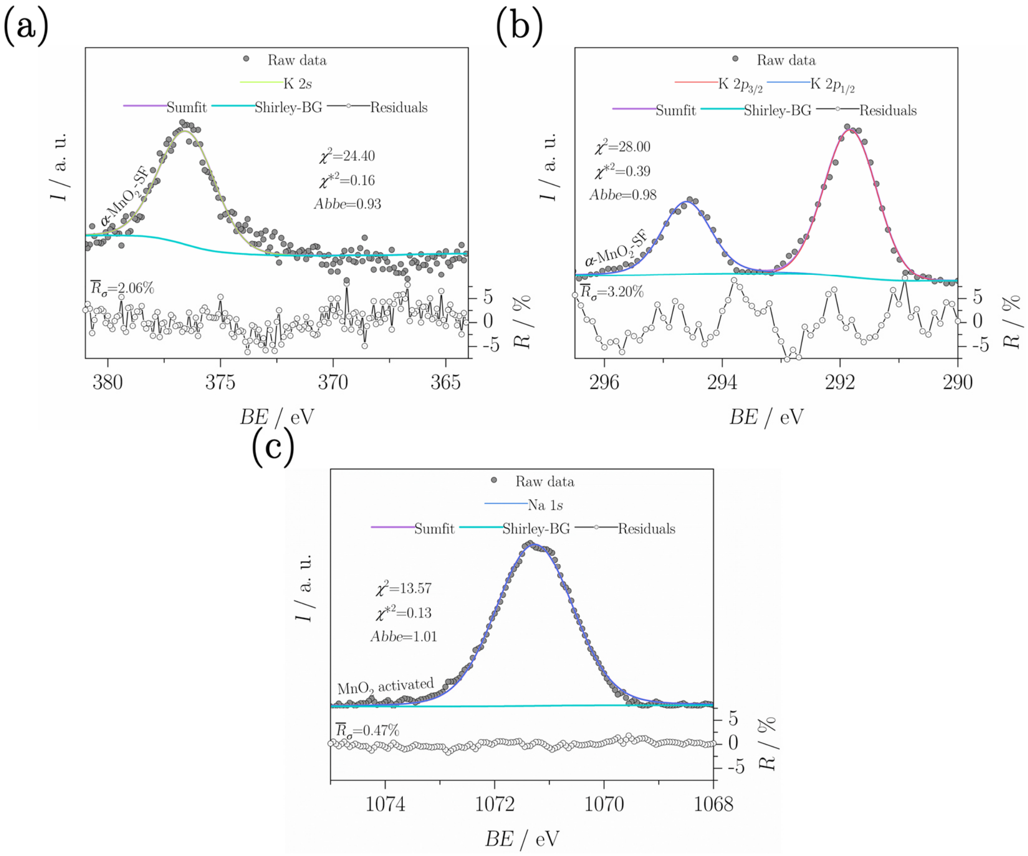

Figure S18. Resolved high-resolution K 2*s*, K 2*p* and Na 1*s* core-level photoemission spectra of reference Mn oxides including percentage residuals and goodness of fit parameters. *BE* positions, *L/G* ratios (not included) and *FWHM* (not included) were used as suggested by Fityk evaluation software. (a) K 2*s* photoemission spectrum of α-MnO_2-SF was fitted using one Voigt line profile at 376.50 eV. (b) K 2$p_{1/2}$ and K 2$p_{3/2}$ photoemission spectra of α-MnO_2-SF were fitted using a total of two Voigt line profiles situated at 294.66 eV and 291.84 eV, respectively. (c) Na 1s photoemission spectrum of commercial MnO_2 activated was resolved by one Voigt line profile located at 1071.27 eV. R, $\overline{R}_{\sigma}$, χ^2, χ^{*2} and *Abbe* ranging from ±5% to ±7.5%, 0.47-3.20%, 13.57-28.00, 0.13-0.39 and 0.93-1.01, respectively, indicating sufficiently accurate fits.

Section S12. Additional goodness of fit parameter of resolved XP spectra

Section S12.1. Mn $2p_{1/2}$ photoemission spectra of as-synthesized α-MnO$_2$

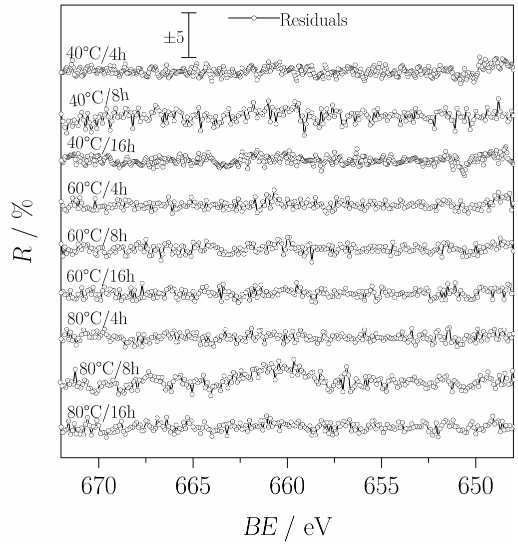

Figure S19. Percentage residuals of resolved high-resolution Mn $2p_{1/2}$ core-level photoemission spectra of as-synthesized α-MnO$_2$ (**Figure S9**). Percentage residuals are in the range of ±2,5% to ±5% indicating sufficiently accurate fits.

Table S17. Summarized goodness of fit parameters, i.e., $\overline{R}_\sigma$, χ^2, χ^{*2} and *Abbe* of resolved high-resolution Mn $2p_{1/2}$ core-level photoemission spectra of as-synthesized α-MnO$_2$ (**Figure S9**). $\overline{R}_\sigma$, χ^2, χ^{*2} and *Abbe* are ranging from 0.71% to 1.18%, 20.57-65.19, 0.08-0.27 and 0.65-1.03, respectively, indicating sufficiently accurate fits.

α-MnO$_2$ / T/t	$\overline{R}_\sigma$ / %	χ^2	χ^{*2}	*Abbe*
40°C/4h	0.75	47.89	0.10	0.69
40°C/8h	1.12	65.19	0.27	0.84
40°C/16h	0.71	54.29	0.11	0.72
60°C/4h	0.74	32.27	0.13	0.91
60°C/8h	0.78	27.05	0.11	0.95
60°C/16h	0.77	28.77	0.12	0.98
80°C/4h	0.72	30.46	0.13	0.96
80°C/8h	1.18	20.57	0.08	0.65
80°C/16h	0.77	30.89	0.13	1.03

Section S12.2. Mn 2$p_{1/2}$ photoemission spectra of reference Mn oxides

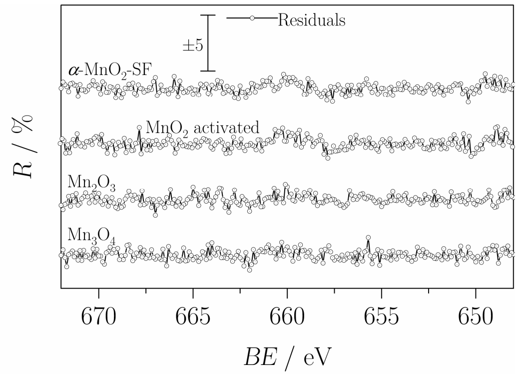

Figure S20. Percentage residuals of resolved high-resolution Mn 2$p_{1/2}$ core-level photoemission spectra of reference Mn oxides (**Figure S10**). Percentage residuals are in the range of ±2,5% to ±5% indicating sufficiently accurate fits.

Table S18. Summarized goodness of fit parameters, i.e., $\overline{R}_{\sigma}$, χ^2, χ^{*2} and *Abbe* of resolved high-resolution Mn 2$p_{1/2}$ core-level photoemission spectra of reference Mn oxides (**Figure S10**). $\overline{R}_{\sigma}$, χ^2, χ^{*2} and *Abbe* are ranging from 0.72 to 0.78%, 30.73-41.24, 0.13-0.17 and 0.90-1.00, respectively, indicating sufficiently accurate fits.

Mn oxide	$\frac{\overline{R}_{\sigma}}{\%}$	χ^2	χ^{*2}	*Abbe*
α-MnO_2-SF	0.73	32.90	0.14	0.97
MnO_2 activated	0.78	41.24	0.17	0.96
Mn_2O_3	0.72	38.11	0.16	1.00
Mn_3O_4	0.74	30.73	0.13	0.90

Section S12.3. Mn 3*s* photoemission spectra of as-synthesized α-MnO$_2$

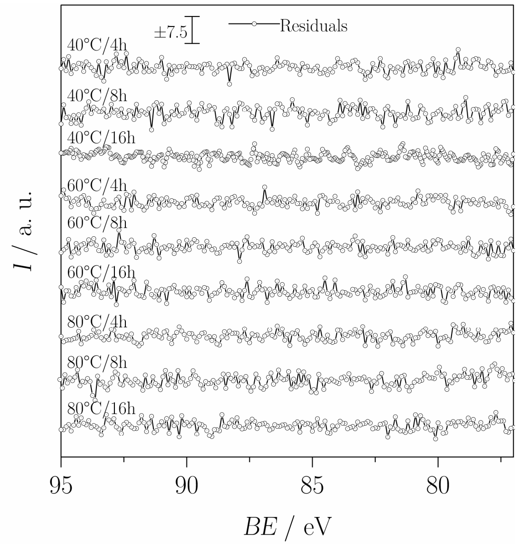

Figure S21. Percentage residuals of resolved high-resolution Mn 3*s* core-level photoemission spectra of as-synthesized α-MnO$_2$ (**Figure S13**). Percentage residuals are in the range of ±5% to ±7.5% indicating suitable fits.

Table S19. Summarized goodness of fit parameters, i.e., $\overline{R}_\sigma$, χ^2, χ^{*2} and *Abbe* of resolved high-resolution Mn 3*s* core-level photoemission spectra of as-synthesized MnO$_2$ (**Figure S13**). $\overline{R}_\sigma$, χ^2, χ^{*2} and *Abbe* are ranging from 2.23% to 3.20%, 12.12-33.92, 0.04-0.19 and 0.97-1.09, respectively, indicating sufficiently accurate fits.

α-MnO$_2$ T/t	$\overline{R}_\sigma$ %	χ^2	χ^{*2}	*Abbe*
40°C/4h	2.61	12.12	0.04	0.99
40°C/8h	3.20	26.89	0.10	0.97
40°C/16h	2.23	23.89	0.06	1.02
60°C/4h	2.37	14.74	0.12	1.02
60°C/8h	2.33	14.50	0.12	1.00
60°C/16h	2.50	22.11	0.14	1.04
80°C/4h	2.36	13.98	0.12	1.09
80°C/8h	2.69	33.92	0.19	1.01
80°C/16h	2.32	14.59	0.11	1.09

Section S12.4. Mn 3*s* photoemission spectra of reference Mn oxides

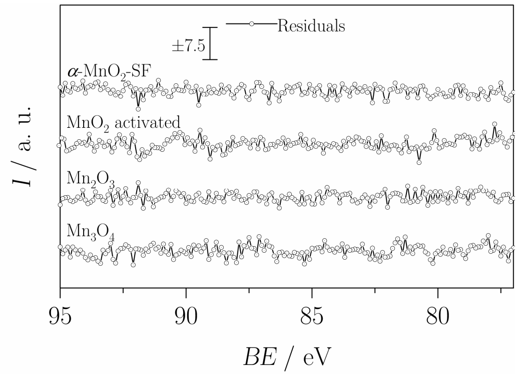

Figure S22. Percentage residuals of resolved high-resolution Mn 3*s* core-level photoemission spectra of reference Mn oxides (**Figure S14**). Percentage residuals are in the range of ±5% to ±7.5% indicating suitable fits.

Table S20. Summarized goodness of fit parameters, i.e., $\overline{R}_\sigma$, χ^2, χ^{*2} and *Abbe* of resolved high-resolution Mn 3*s* core level photoemission spectra of reference Mn oxides (**Figure S14**). $\overline{R}_\sigma$, χ^2, χ^{*2} and *Abbe* are ranging from 2.02% to 2.20%, 15.73-30.17, 0.11-0.14 and 0.96-1.02, respectively, attributing suitable fits.

Mn oxide	$\frac{\overline{R}_\sigma}{\%}$	χ^2	χ^{*2}	*Abbe*
α-MnO_2-SF	2.07	15.73	0.11	0.96
MnO_2 activated	2.19	30.17	0.14	0.99
Mn_2O_3	2.02	26.68	0.13	1.01
Mn_3O_4	2.20	28.67	0.14	1.02

Section S13. Detailed discussion on Mn^{3+} cation defects based on Ag, K and oxygen vacancy contents

Assuming Mn^{3+} cation defects are formed as a result of charge conservation, their contents are too high to have formed exclusively due to interstitial K^+ and Ag^+. However, as described in the manuscript, the emergence of Mn^{3+} cation defects can also be related to the formation of surface oxygen vacancies (and *vice versa*), similarly to the principles of electroneutrality.[24,28–34]

In the framework of a thorough examination the portions of various Mn valences and oxygen species as obtained from the mathematical deconvolution of XP spectra need to be converted to concentrations relative to total elemental compositions of as-synthesized α-MnO_2, i.e., by XPS elemental analysis. (EDX elemental compositions are disregarded, however, since the information depth of EDX is higher compared to XPS,[8] using XPS data is more meaningful here.) Based on the mole fractions of various Mn valences and oxygen species one is able to compute their concentrations relative to total elemental compositions of as-synthesized α-MnO_2 (**Table S21**).

Table S21. Concentrations of K, Ag, H_2O_{ads}, O_{ads}, $O_{lattice}$, Mn^{4+}, Mn^{3+} and Mn^{2+} relative to total elemental compositions of as-synthesized α-MnO2 as obtained by XPS elemental analyses. Concentrations of various oxygen species and Mn valences are computed by conversion of total elemental contents from CasaXPS according to mole fractions from the mathematical deconvolution of respective photoemission spectra.

α-MnO_2	K^a	Ag^b	H_2O_{ads} [c]	O_{ads} [c]	$O_{lattice}$ [c]	$\sum$ K, Ag, O_{ads}	Mn^{4+} [d]	Mn^{3+} [d]	Mn^{2+} [d]
T/t	at.-%	at.-%	at.-%	at.-%	at.-%	at.-%	at.-%	at.-%	at.-%
40°C/4h	1.69	1.25	4.21	13.89	48.48	16.83	13.96	16.35	—
40°C/8h	2.68	0.95	4.50	13.07	47.98	16.70	14.35	16.46	—
40°C/16h	3.28	0.69	2.14	14.63	48.37	18.60	17.44	13.45	—
60°C/4h	3.50	0.59	3.74	12.71	49.41	16.80	15.14	14.95	—
60°C/8h	3.99	0.47	4.17	11.55	49.80	16.01	17.43	11.88	0,71
60°C/16h	4.34	0.37	9.71	11.28	44.21	15.99	16.16	13.33	0,59
80°C/4h	4.33	0.44	1.98	12.57	51.26	17.34	15.40	13.59	0,44
80°C/8h	4.57	0.45	2.34	12.58	49.83	17.60	19.66	10.31	0,24
80°C/16h	2.11	0.47	—	15.76	48.41	18.34	12.39	20.86	—

[a] concentrations by CasaXPS based on K 2*p* spectra (**Table S3**).

[b] concentrations by CasaXPS based on Ag $3d_{5/2}$ spectra (**Table S3**).

[c] concentrations by conversion according to mole fractions by the mathematical deconvolution (**Table S8**) relative to total oxygen contents by CasaXPS (**Table S3**)

[d] concentrations by conversion according to mole fractions by the mathematical deconvolution (**Table S13**) relative to the total manganese contents by CasaXPS (**Table S3**)

As evident from **Table S21**, K and Ag contents are too low to be the sole origin of Mn^{3+} cation defect formation. However, upon assuming the formation of surface Mn^{3+} cation defects to be due to both charge balancing aliovalent dopants as well as surface oxygen vacancies, the totaled concentrations of K, Ag and O$_{\mathrm{ads}}$ ($\sum$ K, Ag, O$_{\mathrm{ads}}$) (7th column) agree very well with concentrations of Mn^{3+} cation defects (9th column).

Minor deviations between $\sum$ K, Ag, O$_{\mathrm{ads}}$ and Mn^{3+} contents can be attributed to different surface sensitivities of various photoemission spectra, what can be readily understood from their inelastic mean free pathways (λ) based on the binding energy positions (BE) of the signals in **Table S22**. Another source of error may lie in the determination of surface oxygen vacancies, the contents of which cannot be exactly quantified since other surface adsorbed oxygen species (with low coordination) are contained within the O$_{\mathrm{ads}}$ components as well.

Table S22. Inelastic mean free pathways (λ) based on binding energy (BE) ranges of Mn 3*s* (main peaks and charge-transfer satellites), K 2*p* (including K 2$p_{3/2}$ and K 2$p_{1/2}$), Ag 3$d_{5/2}$, Mn 2$p_{3/2}$ and Mn 2$p_{1/2}$ (main peaks and charge-transfer satellites) photoemission spectra of as-synthesized α-MnO$_2$. Few material properties of MnO$_2$ used for computations, i.e., bulk density (ρ_{Bulk}=5.03 kg m^{-3}), molar mass (M=86.94·10^{-3} kg mol^{-1}), and number of valence electrons (N_{V}=19) as specified in the QUASES-IMFP-TPP2M software, are indicated. Calculations were carried out using the latest QUASES-IMFP-TPP2M software v3.0 (QUASES Tougaard Inc., Odense SØ, DK, available at QUASES homepage http://www.quases.com/home/)

Spectral feature		$\frac{BE}{\mathrm{eV}}$	$\frac{\lambda}{\text{Å}}$
Mn 3*s*	main peak	83.30-84.45	5.38-5.39
	satellite	88.80-89.30	5.42-5.43
K 2$p_{3/2}$		291.54-291.93	8.70-8.71
K 2$p_{1/2}$		294.35-294.80	8.75-8.76
Ag 3$d_{5/2}$		367.44-364.84	10.04
O 1*s*		529.45-529.90	12.80-12.81
Mn 2$p_{3/2}$		641.75-642.20	14.66-14.67
Mn 2$p_{1/2}$	main peak	653.65-654.00	14.85-14.86
	satellite	664.34-665.88	15.03-15.05

Hence, the formation mechanism of Mn^{3+} cation defects can be attributed to charge conservation resulting from i) the introduction of K^{+} and Ag^{+} into the 2x2 tunnels, i.e., interstitial K^{+}/Ag^{+} in α-MnO$_2$, ii) but predominantly from the formation of surface oxygen vacancies.

Section S14. Additional ORR activity metrics of as-synthesized α-MnO$_2$

Table S23. Summarized half-wave potentials ($E_{1/2}$), potentials at -3 mA $\mathrm{cm}_{\mathrm{GC}}^{-2}$ ($E_{j=-3}$), diffusion-limiting current densities (j_L) and kinetic current densities (j_k) of as-synthesized α-MnO$_2$ catalysts as obtained from thin-film rotating disk electrode (TF-RDE) measurements.

α-MnO$_2$ / T/t	$E_{1/2}$ [a] / V	$E_{j=-3}$ [a] / V	j_L / mA $\mathrm{cm}_{\mathrm{GC}}^{-2}$	j_k / mA $\mathrm{cm}_{\mathrm{GC}}^{-2}$
40°C/4h	-0.43	-0.62	-3.33	0.32
40°C/8h	-0.20	-0.23	-4.90	5.03
40°C/16h	-0.24	-0.46	-3.56	0.99
60°C/4h	-0.22	-0.28	-4.53	2.78
60°C/8h	-0.22	-0.36	-4.20	1.81
60°C/16h	-0.23	-0.24	-4.90	3.17
80°C/4h	-0.19	-0.20	-5.02	7.61
80°C/8h	-0.20	-0.23	-4.51	3.33
80°C/16h	-0.36	-0.39	-4.57	0.90

[a] vs. Ag/AgCl (sat. KCl)

Section S15. N_2 adsorption-desorption measurements of as-synthesized α-MnO_2

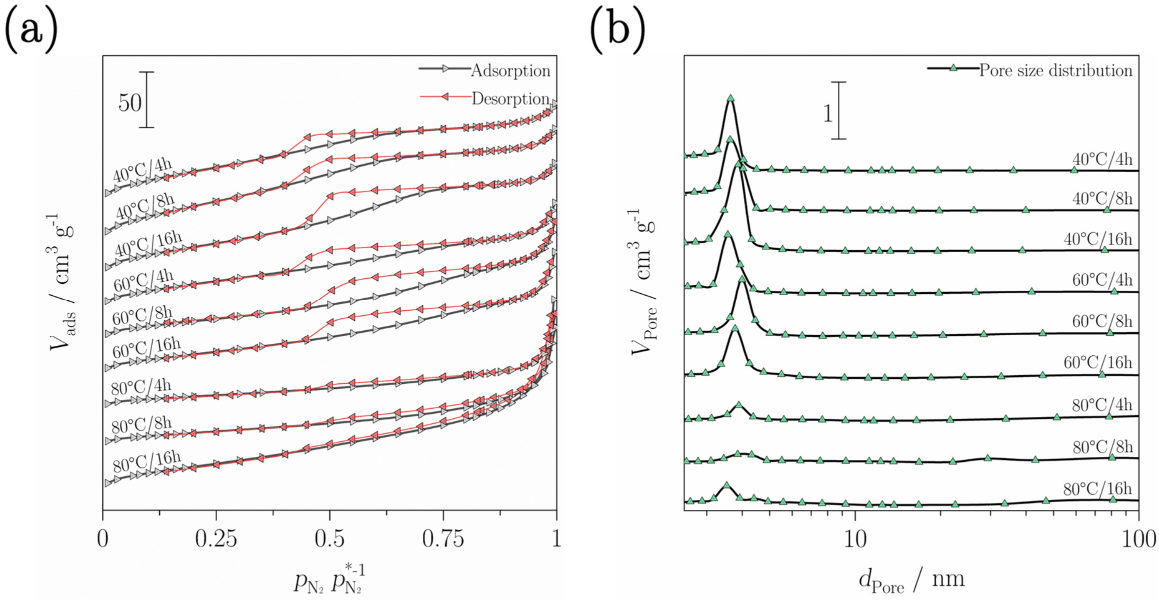

Figure S24. (a) N_2 adsorption-desorption isotherms and (b) Barrett-Joyner-Halenda (BJH) pore size distribution (PSD) curves of as-synthesized MnO_2. Note, isotherms and PSDs are vertically shifted for clarity.

Table S24. Summarized Brunauer, Emmett and Teller (BET) specific surface areas (BET *SA*), modal pore diameters (d_{Pore}) from BJH pore size distribution curves, BJH average pore diameters ($\bar{d}_{Pore}$) and BJH cumulative pore volumes (V_{Pore}) as obtained from N_2 adsorption-desorption measurements of as-synthesized α-MnO_2 (**Figure S24**).

α-MnO_2	BET *SA*	d_{Pore}	$\bar{d}_{Pore}$	V_{Pore}
T/t	m^2 g^{-1}	nm	nm	cm^3 g^{-1}
40°C/4h	184.0	3.6	4.0	0.19
40°C/8h	214.6	3.6	3.9	0.22
40°C/16h	171.6	3.9	4.1	0.20
60°C/4h	142.1	3.6	4.8	0.19
60°C/8h	125.5	4.0	6.0	0.18
60°C/16h	117.2	3.8	5.9	0.20
80°C/4h	69.4	3.9	9.3	0.15
80°C/8h	70.9	3.9	9.6	0.18
80°C/16h	98.2	3.5	8.3	0.30

Generally, all as-synthesized α-MnO_2 exhibit pore condensation and hysteresis, that is indicative for the presence of mesopores (**Figure S24a**).[35] MnO_2 synthesized at 40°C/4h to 60°C/16h exhibit a typical type IV(a) isotherm according to UPAC classification.[36]

Moreover, they are accompanied by H2(b) type hysteresis loops, which are characterized by a descending desorption branch in consequence of partial network and pore blocking mechanisms during the desorption.[37,38] Furthermore, by increasing temperature and dwell time of the synthesis capillary condensation is shifted to higher relative pressures, i.e., from ~0.65 to ~0.9, thus indicating increasing mesopore diameters. This is in good agreement with the modal pore diameters as obtained from PSD curves demonstrating a unimodal pore size distribution as well as BJH mean average pore diameters (**Table S24**). Furthermore, the (single) maxima in the PSD curves are narrow (**Figure S24b**), that is indicative of ordered materials possessing well defined pore geometry.[38] Contrary, for α-MnO_2 samples synthesized at 80°C, wide but less pronounced hysteresis loops exhibiting parallel adsorption and desorption branches can be observed.[38] The adsorption branches display a hybrid of type I and type IV isotherms accompanied by a composite of H3 and H4 hysteresis loops. Additionally, a slight cavitation step can be identified within the desorption branches appearing at relative pressures of 0.45 to 0.55, that is indicative for the presence of mesopores of a size ca. ≤5 nm.[37] Capillary condensation occurring at high relative pressures likewise indicate the presence of larger mesopores.[39] Moreover, though the PSD curves still present a unimodal distribution each, i.e., a single maximum in the mesoporous range, the discrepancy between d_{Pore} and $\bar{d}_{\text{Pore}}$ can be considered an indication for larger mesopores as well. Furthermore, cumulative pore volumes likewise demonstrate a trend similar to what is ascertainable for other porosity features. Eventually, this leads to the assumption that mesoporosity mainly originates from the microspheres (core), while the spike-shells consisting of less densely arranged primary particles as compared to microspheres provide larger pores as well as additional (cumulative) pore volume. BET *SA*s of as-synthesized α-MnO_2 are roughly decreasing with temperature and dwell time of the synthesis. However, this can be explained by a formation of denser structures due to an accelerated nucleation as well as precipitating of α-MnO_2 within the pores instead of collaborating to a progressive formation of a mesoporous structure.

Section S16. Double-layer capacitance measurements of pure acetylene carbon black thin-films with various mass-loadings

Section S16.1. 50 μg_{AB} cm_{GC}^{-2}

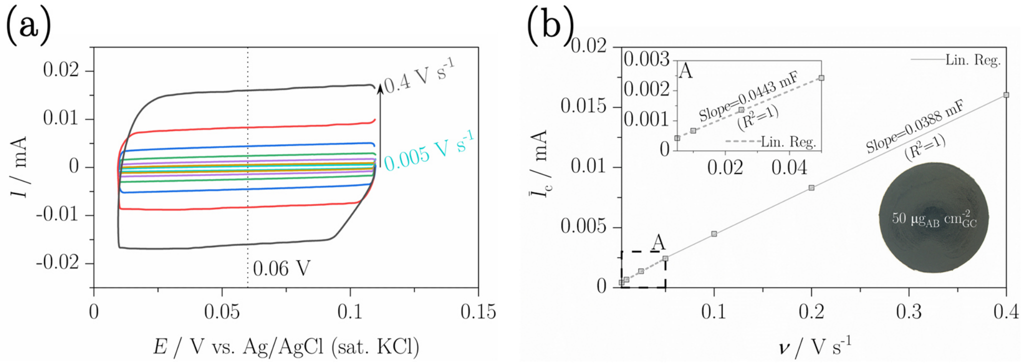

Figure S25. Double-layer capacitance measurement of a pure acetylene carbon black (AB) thin-film with a mass-loading of 50 µg cm_{GC}^{-2}. (a) Cyclic voltammograms (CVs) measured at various potential scan-rates, i.e., 0.005, 0.01, 0.025, 0.05, 0.1, 0.2 and 0.4 V s^{-1}, in N_2 saturated, 0.1 M KOH aqueous electrolyte under static conditions (0 rpm). Prior to measurements, the electrolyte was equilibrated to 25°C for 30 min. CVs were measured in the non-Faradaic potential region, i.e., a ±0.05 V potential window centered on the open circuit potential (*OCP*). Subsequently, *OCP* was recorded for 30 min (not included) and determined to be 0.06 V (vs. Ag/AgCl (sat. KCl)). (b) Capacitive currents ($\bar{I}_c$), i.e., average of anodic and cathodic capacitive currents at 0.06 V (vs. Ag/AgCl (sat. KCl)), as a function of potential scan-rates (*v*). A 1st linear regression line representing the total double-layer capacitance ($C_{dl,\ total}$) was applied to the data within a 0.005-0.05 V s^{-1} potential scan-rate range (**Figure S25b** inset), while a 2nd linear regression line belonging to the outer double-layer capacitance ($C_{dl,\ outer}$) is obtained in a potential scan-rate range from 0.05-0.4 V s^{-1}. Subsequently, the slopes of regression lines give a $C_{dl,\ total}$ and $C_{dl,\ outer}$ of 0.0443 mF and 0.0388 mF, respectively.

Section S16.2. 150 μg_{AB} cm_{GC}^{-2}

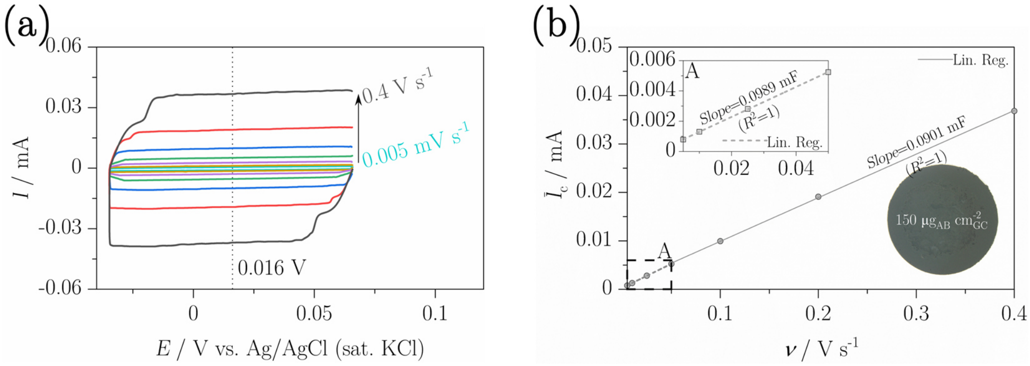

Figure S26. Double-layer capacitance measurement of a pure AB thin-film with a mass-loading of 150 µg cm_{GC}^{-2}. (a) CVs measured at various potential scan-rates, i.e., 0.005, 0.01, 0.025, 0.05, 0.1, 0.2 and 0.4 V s^{-1}, in N_2 saturated, 0.1 M KOH aqueous electrolyte under static conditions (0 rpm). Prior to measurements, the electrolyte was equilibrated to 25°C for 30 min. CVs were measured in the non-Faradaic potential region, i.e., a ±0.05 V potential window centered on the *OCP*. Subsequently, *OCP* was recorded for 30 min (not included) and determined to be 0.016 V (vs. Ag/AgCl (sat. KCl)). (b) Capacitive currents ($\bar{I}_c$), i.e., average of anodic and cathodic capacitive currents at 0.016 V (vs. Ag/AgCl (sat. KCl)), as a function of potential scan-rates (v). A 1st linear regression line representing $C_{dl,\ total}$ was applied to the data within a 0.005-0.05 V s^{-1} potential scan-rate range (**Figure S26b** inset), while a 2nd linear regression line belonging to $C_{dl,\ outer}$ is obtained in a potential scan-rate range from 0.05-0.4 V s^{-1}. Subsequently, the slopes of regression lines give a $C_{dl,\ total}$ and $C_{dl,\ outer}$ of 0.0989 mF and 0.0901 mF, respectively.

Section S16.3. $300\ \mu g_{AB}\ cm^{-2}_{GC}$

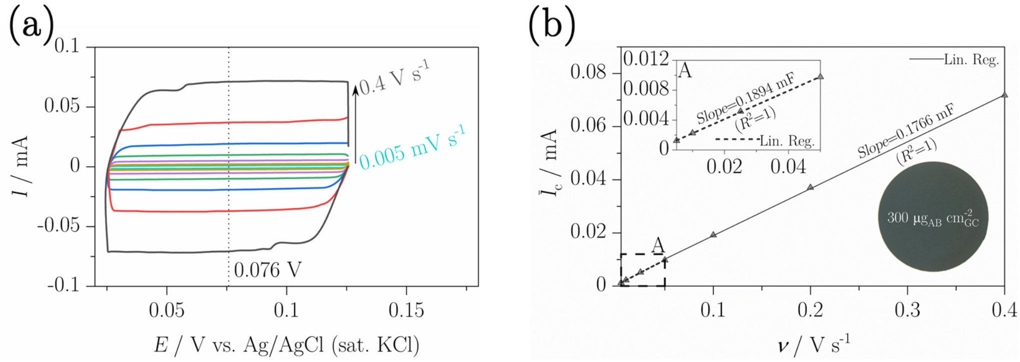

Figure S27. Double-layer capacitance measurement of a pure AB thin-film with a mass-loading of 300 µg cm^{-2}_{GC}. (a) CVs measured at various potential scan-rates, i.e., 0.005, 0.01, 0.025, 0.05, 0.1, 0.2 and 0.4 V s^{-1}, in N_2 saturated, 0.1 M KOH aqueous electrolyte under static conditions (0 rpm). Prior to measurements, the electrolyte was equilibrated to 25°C for 30 min. CVs were measured in the non-Faradaic potential region, i.e., a ±0.05 V potential window centered on the *OCP*. Subsequently, *OCP* was recorded for 30 min (not included) and determined to be 0.076 V (vs. Ag/AgCl (sat. KCl)). (b) Capacitive currents ($\bar{I}_c$), i.e., average of anodic and cathodic capacitive currents at 0.076 V (vs. Ag/AgCl (sat. KCl)), as a function of potential scan-rates. A 1st linear regression line representing $C_{dl,\ total}$ was applied to the data within a 0.005-0.05 V s^{-1} potential scan-rate range (**Figure S27b** inset), while a 2nd linear regression line belonging to $C_{dl,\ outer}$ is obtained in a potential scan-rate range from 0.05-0.4 V s^{-1}. Subsequently, the slopes of regression lines give a $C_{dl,\ total}$ and $C_{dl,\ outer}$ of 0.1894 mF and 0.1766 mF, respectively.

Section S16.4. 600 μg_{AB} cm^{-2}_{GC}

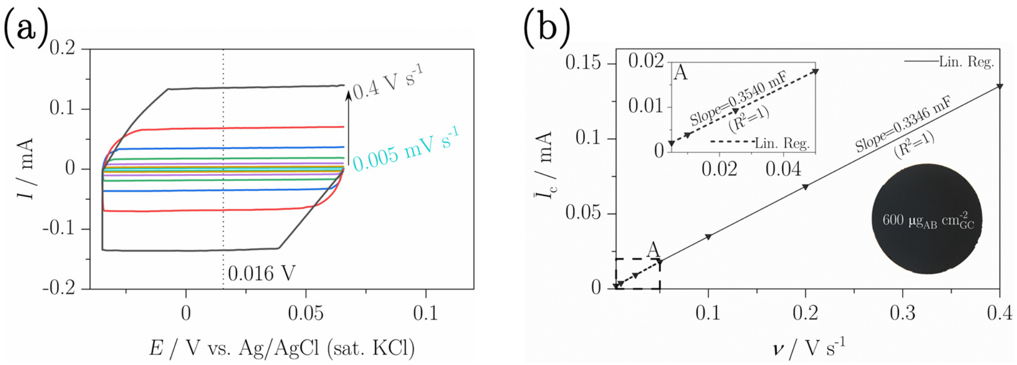

Figure S28. Double-layer capacitance measurement of a pure AB thin-film with a mass-loading of 600 μg cm^{-2}_{GC}. (a) CVs measured at various potential scan-rates, i.e., 0.005, 0.01, 0.025, 0.05, 0.1, 0.2 and 0.4 V s^{-1}, in N_2 saturated, 0.1 M KOH aqueous electrolyte under static conditions (0 rpm). Prior to measurements, the electrolyte was equilibrated to 25°C for 30 min. CVs were measured in the non-Faradaic potential region, i.e., a ±0.05 V potential window centered on the *OCP*. Subsequently, *OCP* was recorded for 30 min (not included) and determined to be 0.016 V (vs. Ag/AgCl (sat. KCl)). (b) Capacitive currents ($\bar{I}_c$), i.e., average of anodic and cathodic capacitive currents at 0.016 V (vs. Ag/AgCl (sat. KCl)), as a function of potential scan-rates. A 1st linear regression line representing $C_{dl,\ total}$ was applied to the data within a 0.005-0.05 V s^{-1} potential scan-rate range (**Figure S28b** inset), while a 2nd linear regression line belonging to $C_{dl,\ outer}$ can be applied in potential scan-rate range from 0.05-0.4 V s^{-1}. Subsequently, the slopes of regression lines give a $C_{dl,\ total}$ and $C_{dl,\ outer}$ of 0.3540 mF and 0.3346 mF, respectively.

Section S16.5. Summary of double-layer capacitances of acetylene carbon black thin-films with various mass-loadings

Table S25. Summarized double-layer capacitances of AB thin-films with various mass-loadings, i.e., 50, 150, 300, and 600 µg $\mathrm{cm}^{-2}_{\mathrm{GC}}$. $C_{\mathrm{dl,\ total}}$ and $C_{\mathrm{dl,\ outer}}$ are derived from the slopes of linear regression lines to capacitive currents ($\bar{I}_{\mathrm{C}}$) in a potential scan-rate range of 0.005-0.05 V s^{-1} (1st slope) and 0.05-0.4 V s^{-1} (2nd slope), respectively. The inner double-layer capacitance ($C_{\mathrm{dl,\ inner}}$) is calculated based on $C_{\mathrm{dl,\ inner}}=C_{\mathrm{dl,\ total}}-C_{\mathrm{dl,\ outer}}$. Moreover, the percentage of each double-layer capacitance constituent is indicated.

m_{AB}	$C_{\mathrm{dl,\ total}}$ [a]	$C_{\mathrm{dl,\ outer}}$		$C_{\mathrm{dl,\ inner}}$ [b]	
µg $\mathrm{cm}^{-2}_{\mathrm{GC}}$	mF	mF	%	mF	%
50	0.0443	0.0388	87.58	0.0055	12.42
150	0.0989	0.0901	91.10	0.0088	8.90
300	0.1894	0.1766	93.24	0.0128	6.76
600	0.3540	0.3346	94.52	0.0194	5.48

[a] $C_{\mathrm{dl,\ total}} \triangleq 100\%$

[b] $C_{\mathrm{dl,\ inner}}=C_{\mathrm{dl,\ total}}-C_{\mathrm{dl,\ outer}}$

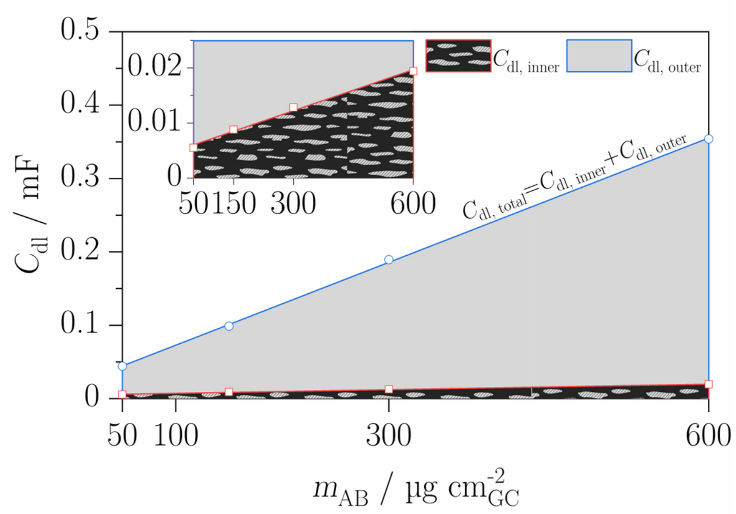

Figure S29. Graphical summary of double-layer capacitances measured on pure AB thin-films with various mass-loadings, i.e., 50, 150, 300, and 600 µg $\mathrm{cm}^{-2}_{\mathrm{GC}}$. $C_{\mathrm{dl,\ inner}}$ and $C_{\mathrm{dl,\ outer}}$ are represented through a light-grey and bony coal textured area, respectively, while $C_{\mathrm{dl,\ total}}$ can be regarded the sum of these two areas, i.e., $C_{\mathrm{dl,\ total}}=C_{\mathrm{dl,\ inner}}+C_{\mathrm{dl,\ outer}}$. The inset shows a magnified representation of $C_{\mathrm{dl,\ inner}}$. However, the double layer capacitances demonstrate a linear increase with increasing the AB mass-loading.

Section S17. Additional data on double-layer capacitance and electrochemically active surface area (*ECSA*) measurements of α-MnO$_2$-acetylene carbon black (AB) thin-films

Section S17.1. Double layer capacitances of complete α-MnO$_2$-AB thin-films and correction for the contribution of AB conductive support

Table S26. Summarized double-layer capacitances of complete α-MnO$_2$-AB thin-films and correction for the contribution of AB conductive supports. Total ($C_{\mathrm{dl,\ total}}^{*}$) and outer double-layer capacitances of complete thin-films ($C_{\mathrm{dl,\ outer}}^{*}$) are derived from the slopes of linear regression lines to capacitive currents ($\bar{I}_c$) in a potential scan-rate range of 0.005-0.05 V s^{-1} (1st slope) and 0.05-0.4 V s^{-1} (2nd slope), respectively. Individual double-layer capacitances, i.e., corrected for the contribution of AB conductive supports, were determined by substracting $C_{\mathrm{dl,\ total}}$ and $C_{\mathrm{dl,\ outer}}$ of a pure AB thin-film with a mass-loading of 50 µg $\mathrm{cm}_{\mathrm{GC}}^{-2}$ from double-layer capacitances of complete thin-films. Inner double-layer capacitances are calculated based on $C_{\mathrm{dl,\ inner}}=C_{\mathrm{dl,\ total}}-C_{\mathrm{dl,\ outer}}$. Moreover, the percentage of each corrected double-layer capacitance constituent is indicated.

α-MnO$_2$	$C_{\mathrm{dl,\ total}}^{*}$	$C_{\mathrm{dl,\ outer}}^{*}$	$C_{\mathrm{dl,\ total}}^{a,b}$	$C_{\mathrm{dl,\ outer}}^{b}$		$C_{\mathrm{dl,\ inner}}^{c}$	
T/t	mF	mF	mF	mF	%	mF	%
40°C/4h	0.0605	0.0523	0.0162	0.0135	83.33	0.0027	16.67
40°C/8h	0.1265	0.0597	1.1591	0.2947	25.42	0.8644	74.58
40°C/16h	0.0849	0.0541	0.5725	0.2157	37.68	0.3568	62.32
60°C/4h	0.1246	0.0518	1.1323	0.1833	16.19	0.9490	83.81
60°C/8h	0.3224	0.0751	3.9214	0.5119	13.05	3.4096	86.95
60°C/16h	0.1647	0.0567	1.6977	0.2524	14.87	1.4453	85.13
80°C/4h	0.2188	0.0512	2.4606	0.1749	7.11	2.2857	92.89
80°C/8h	0.6240	0.1168	8.1742	1.0999	13.46	7.0743	86.54
80°C/16h	0.5515	0.1134	7.1519	1.0519	14.71	6.100	85.29

*Double-layer capacitance of complete α-MnO$_2$-acetylene carbon black (AB) thin-films.

[a] $C_{\mathrm{dl,\ total}} \triangleq 100\%$

[b] Double-layer capacitance corrected for the contribution of 50 µg $\mathrm{cm}_{\mathrm{GC}}^{-2}$ AB conductive support based on $C_{\mathrm{dl,\ \alpha\text{-}MnO_2}}=C_{\mathrm{dl}}^{*}-C_{\mathrm{dl,\ AB}}$, where $C_{\mathrm{dl,\ total\ AB}}=0.0443$ mF and $C_{\mathrm{dl,\ outer\ AB}}=0.0388$ mF.

[c] $C_{\mathrm{dl,\ inner}}=C_{\mathrm{dl,\ total}}-C_{\mathrm{dl,\ outer}}$

Section S17.2. *ECSA*s of individual α-MnO_2 catalysts

Table S27. Summarized individual *ECSA*s of as-synthesized α-MnO_2 catalysts. *ECSA*s are calculated from double-layer capacitances corrected for the contribution of 50 µg cm^{-2}_{GC} AB conductive supports and the areal capacitance of a bare GC disk electrode considered a specific double-layer capacitance (C_s=0.0709 mF cm^{-2}), as previously described.[40] Moreover, the percentage of each *ECSA* constituent is indicated.

α-MnO_2	$ECSA_{total}$ [a]	$ECSA_{inner}$ [b]		$ECSA_{outer}$ [b]	
T/t	cm^2	cm^2	%	cm^2	%
40°C/4h	0.23	0.04	16.67	0.19	83.33
40°C/8h	1.16	0.86	74.58	0.29	25.42
40°C/16h	0.57	0.36	62.32	0.22	37.68
60°C/4h	1.13	0.95	83.81	0.18	16.19
60°C/8h	3.92	3.41	86.95	0.51	13.05
60°C/16h	1.70	1.45	85.13	0.25	14.87
80°C/4h	2.46	2.29	92.89	0.17	7.11
80°C/8h	8.17	7.07	86.54	1.10	13.46
80°C/16h	7.15	6.10	85.29	1.05	14.71

[a] $ECSA_{total} \triangleq 100\%$

Section S18. Detailed structural and physicochemical characterization of reference Mn oxides

Section S18.1. PXRD structural analysis

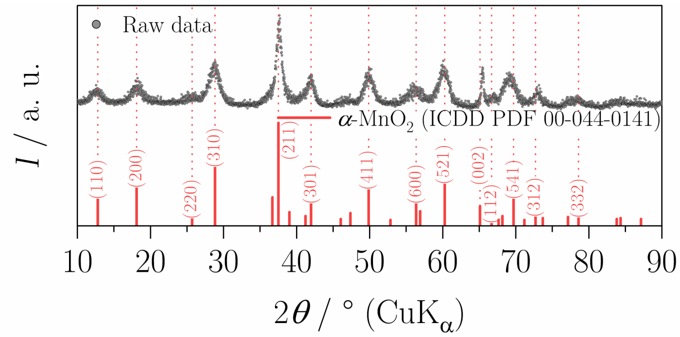

Figure S30. PXRD reflection pattern of α-MnO$_2$-SF. Reflections observed at angles 2θ 12.78°, 18.11°, 25.71°, 28.84°, 37.52°, 41.97°, 49.87°, 56.37°, 60.28°, 65.11°, 66.69°, 69.71°, 72.71° and 78.59° can be well indexed to the (1 1 0), (2 0 0), (2 2 0), (3 1 0), (2 1 1), (3 0 1), (4 1 1), (6 0 0), (5 2 1), (0 0 2), (1 1 2), (5 4 1), (3 1 2) and (3 3 2) crystallographic planes of tetragonal α-MnO$_2$ (ICDD PDF 00-044-0141, space group I4/m, a=b=9.7847 Å, c=2.8630 Å).[40–42] No impurity reflections are observable in the PXRD reflection pattern, indicating a high purity of α-MnO$_2$-SF. (Note, it is already referred to as α-MnO$_2$-SF in the manuscript as well as supporting information).

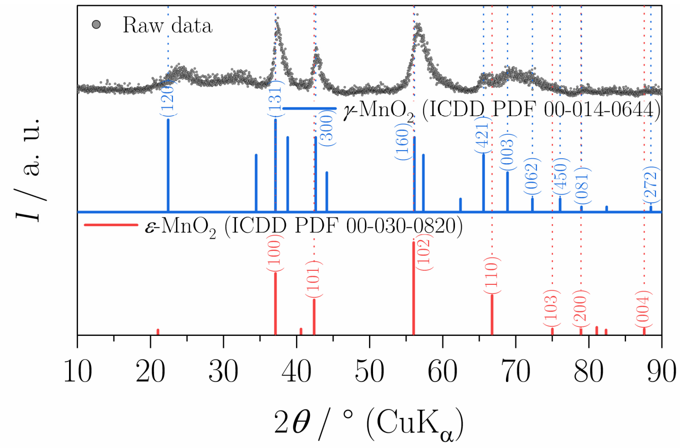

Figure S31. PXRD reflection pattern of commercial MnO_2 activated. The experimental PXRD reflection pattern fits well with hexagonal ε-MnO_2 (ICDD PDF 00-030-0820, space group P63/mmc, a=b=2.8 Å, c=4.45 Å).[43,44] Moreover, good correspondence with orthorhombic γ-MnO_2 (ICDD PDF 00-014-0644, a=6.36 Å, b=10.15 Å, c=4.09 Å) could be obtained as well[45,46] indicating a mixed ε-/γ-phase.[47,48] While major reflections observed at 2θ 37.15°, 42.73° and 56.53°, as well as a weak reflection at ~78.93°2θ, can be related to the (1 0 0), (1 0 1), (1 0 2), and (2 0 0) as well as (1 3 1), (3 0 0), (1 6 0) and (0 8 1) crystallographic planes of ε- and γ-MnO_2, respectively, reflections at 2θ ~65.37°, ~68.59° and ~72.63° are exclusively assignable to the (4 2 1), (0 0 3) and (0 6 2) crystallographic planes of γ-MnO_2. Furthermore, in the low angles 2θ region a broad reflection, which is split into two diffraction peaks, is observable. Considering a marked shift of a nearly 1.5°2θ towards higher angles 2θ as compared to pristine γ-MnO_2 ($2\theta_{(1\,2\,0)}$=22.42°), that does not occur for the other reflections, the 1st diffraction peak at ~23.89°2θ cannot be related to the (1 2 0) crystallographic plane of γ-MnO_2. However, according to Chabre et al. and Sokolsky et al., it might arise from microtwinning, or an random intergrowth of two other MnO_2 polymorphs, i.e., ramsdellite and pyrolysute.[49,50] The 2nd diffraction peak is located at ~33.11°2θ. Similar could be observed by Kim et al., but after heat treating ε-MnO_2 samples at various temperatures >200°C: They found a splitting of an originally single broad reflection located at 21.3°2θ into two diffraction peaks, the angular positions of which are comparable to the present 1st and 2nd diffraction peaks.[44] Though we do not know the synthesis route of commercial MnO_2 activated, or how the activation process was carried out, respectively, the latter indeed traditionally involves, inter alia, a successive thermal treatment at elevated temperatures for removal of water (drying).[51] The splitting of the broad reflection in the low angles 2θ region is therefore very likely to be a consequence of a thermal treatment during the activation process of MnO_2. (It is to be noted that this sample is still referred to as MnO_2 activated in the manuscript as well as supporting information).

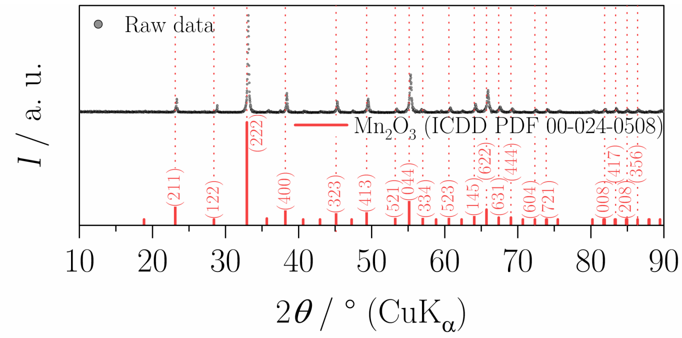

Figure S32. PXRD reflection pattern of commercial Mn_2O_3. Reflections observed at angles 2*θ* 23.12°, 28.42°, 32.92°, 38.2°, 45.14°, 49.32°, 55.14°, 64.06°, 65.72°, 67.4° as well as weak reflection located at 53.24°, 57°, 60.58°, 69.06°, 72.34°, 73.9°, 81.88°, 83.4°, 84.96° and 86.41° can be well indexed to the (2 1 1), (1 2 2), (2 2 2), (4 0 0), (3 2 3), (4 1 3), (0 4 4), (1 4 5), (6 2 2), (6 3 1), (3 5 6), (5 2 1), (3 3 4), (5 2 3) (4 4 4), (6 0 4), (7 2 1), (0 0 8), (4 1 7) and (2 0 8) crystallographic planes of orthorhombic spinel Mn_2O_3 (ICDD PDF 00-024-0508, space group Pcab, a=9.4161 Å, b=9.4237 Å, c=9.4051 Å).[52–54] As no characteristic reflections of other phases can be identified, commercial Mn_2O_3 can be considered to be of high purity.

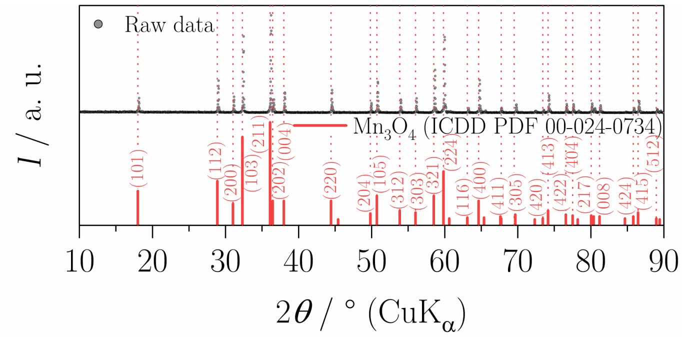

Figure S33. PXRD reflection pattern of commercial Mn_3O_4. Reflections observed at angles 2*θ* 18°, 28.88, 31.02°, 32.32°, 36.09°, 36.45°, 37.98°, 44.44°, 49.82°, 50.71°, 53.86°, 56.01°, 58.51°, 59.84°, 64.65°, 69.66°, 74.15°, 76.58°, 77.51°, 80.05°, 81.21°, 86.47° as well as weak reflections located at 63.1°, 67.73°, 73.44°, 85.8° and 88.97° can be well indexed to the (1 0 1), (1 1 2), (2 0 0), (1 0 3), (2 1 1), (2 0 2), (0 0 4), (2 2 0), (2 0 4), (1 0 5), (3 1 2), (3 0 3), (3 2 1), (2 2 4), (4 0 0), (3 0 5), (4 1 3), (4 2 2), (4 0 4), (2 1 7), (0 0 8), (4 1 5), (1 1 6), (4 1 1), (4 2 0), (4 2 4) and (5 1 2) crystallographic planes of tetragonal spinel Mn_3O_4 (ICDD PDF 00-024-0734, space group I41/amd, a=b=5.7621 Å, c=9.4696 Å).[55–57] No characteristic reflections of other phases are observed in the PXRD reflection pattern, suggesting commercial Mn_3O_4 to be of high purity.

Section S18.2. SEM evaluation and morphological features

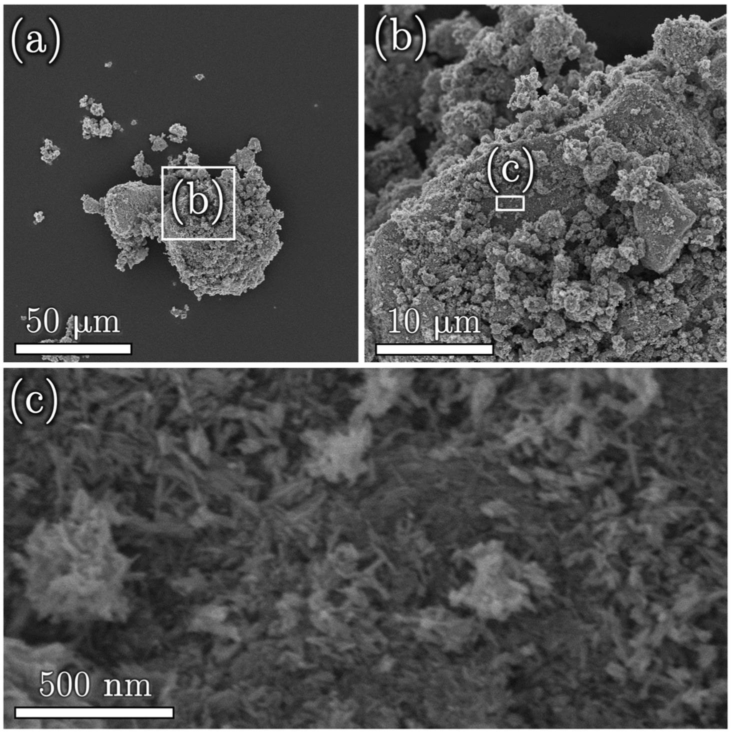

Figure S34. SEM evaluation of α-MnO_2-SF. (a) Overview, (b) a magnified aggregate and (c) higher magnification of fiber-like primary particles. The fibers are in the nanometer range, however, diameters and lengths of fibers were not determinable.

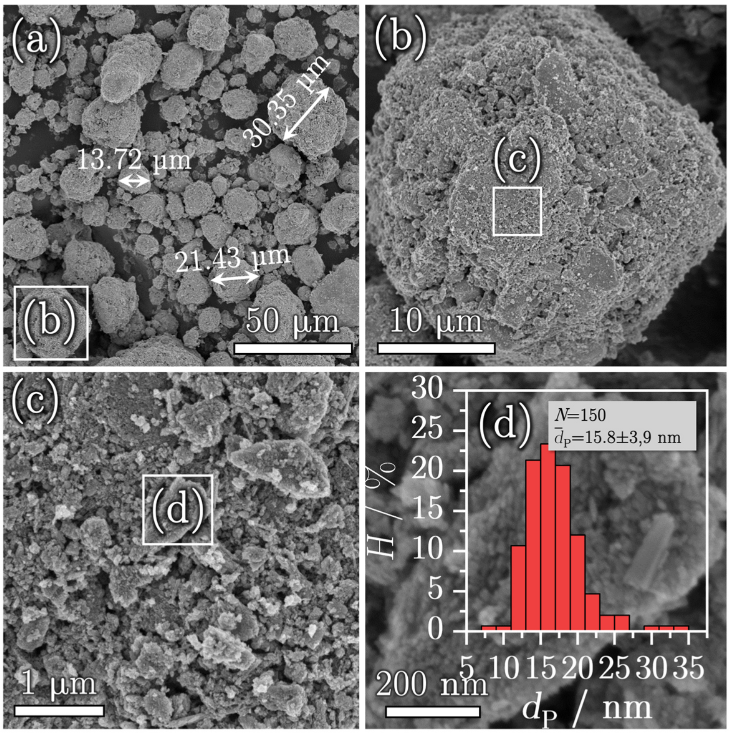

Figure S35. SEM evaluation of commercial MnO_2 activated. (a) Overview of agglomerates. Diameters of three representative agglomerates are indicated ranging from 13.72 µm to 30.35 µm. (b), (c) A magnified agglomerate and (d) higher magnification of nanometer-sized, spherical primary particles (nanoparticles) including the particle size distribution (modal and mean particles sizes) of primary particles based on evaluation of 150 particles.

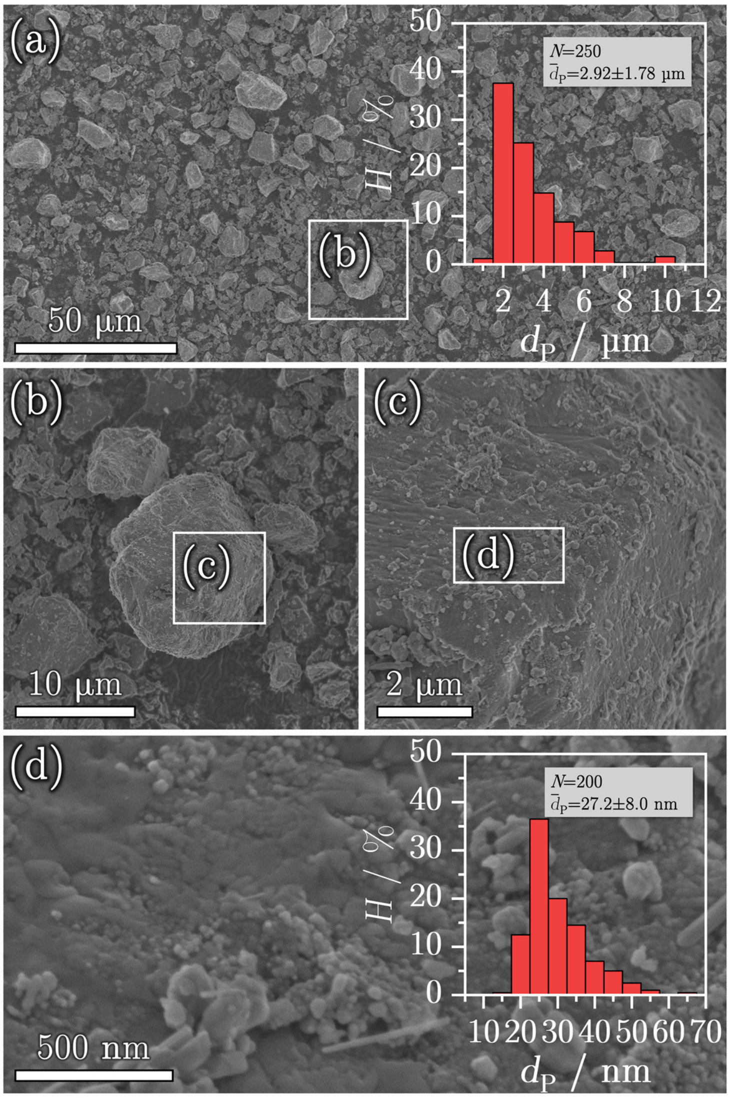

Figure S36. SEM evaluation of commercial Mn_2O_3. (a) Overview, (b), (c) magnified agglomerates and (d) higher magnification of nanometer-sized, spherical primary particles including the particle size distribution (modal and mean particle size) of primary particles based on evaluation of 200 particles.

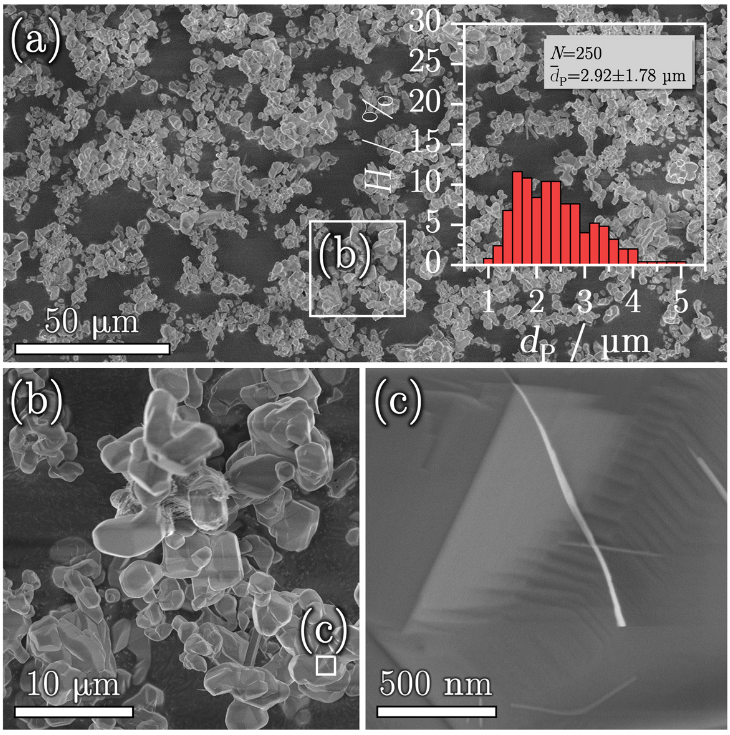

Figure S37. SEM evaluation of commercial Mn_3O_4. (a) Overview including the particle size distribution (modal and mean particle size) based on evaluation of 250 particles, (b) magnified irregular truncated polyhedron-like particles and (c) higher magnification of a particle surface.

α-MnO_2-SF shows huge aggregates, one of which is presented in the SEM image in **Figure S34a**. A higher magnification reveals loosely-stacked agglomerates (**Figure S34b**), whose primary morphology in turn adapts short fibers (SF) (**Figure S34c**), the diameters of which are in the nanometer range (denoted α-MnO_2-SF). Similar applies to commercial MnO_2 activated (**Figure S35**) and commercial Mn_2O_3 agglomerates (**Figure S36**), but consisting of nanometer-sized, spherical particles. While the size of commercial MnO_2 activated nanoparticles could be measured to be d_P=16 nm and $\bar{d}_P$=15.8±3.9 nm (based on evaluation of 150 particles) (**Figure S35d**), commercial Mn_2O_3 nanoparticles are slightly enlarged (d_P=25 nm, $\bar{d}_P$=27.2±8.0 nm) (based on evaluation of 200 particles) as well as more densely coalesced (**Figure S36d**). In contrast, commercial mixed valence Mn_3O_4 adapts irregular truncated polyhedron-like shapes (**Figure S37b**) with considerable inhomogeneous particle sizes ranging from ~1.4 µm to ~2.8 µm as well as 2.28±0.77 µm for the modal and mean particle sizes (based on evaluation of 250 particles) (**Figure S37a**), respectively. A higher magnification SEM image (**Figure S37c**) does not reveal primary particles, but smooth surfaces patterned by nano-scale tiers or strata are observable.

Section S18.3. SEM-EDX elemental analysis

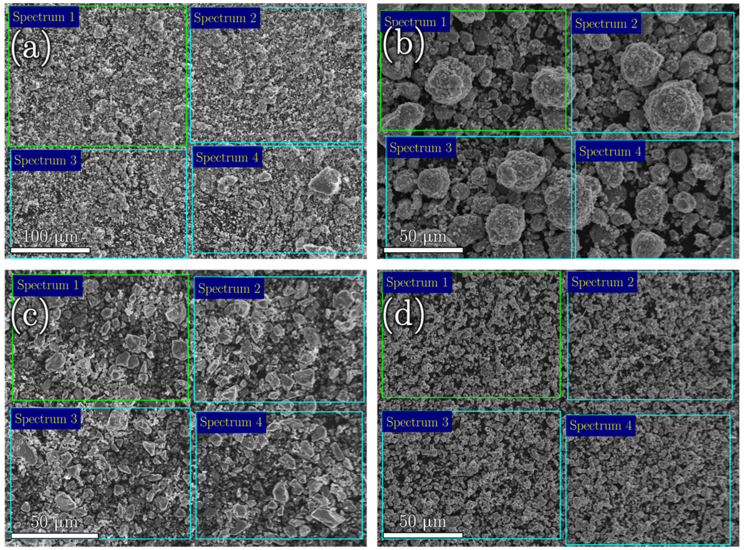

Figure S38. SEM-EDX area analysis of reference Mn oxides at 15 kV acceleration voltage. (a) α-MnO_2-SF at 250x magnification and (b) commercial MnO_2 activated, (c) commercial Mn_2O_3 and (d) commercial Mn_3O_4 at 500x magnification. Green and cyan squares mark the areas where EDX was carried out.

Table S28. Summarized SEM-EDX elemental compositions of Mn, O, K and Na measured at 250x (α-MnO_2-SF), or 500x magnification (commercial MnO_2 activated, Mn_2O_3 and Mn_3O_4), respectively, and 15 kV acceleration voltage. C was deducted from EDX spectra as carbon sputter coating was applied for preparing the samples and the samples were fixed on carbon tabs.

Mn oxide	Spectrum 1				Spectrum 2				Spectrum 3				Spectrum 4			
	Mn	O	K	Na	Mn	O	K	Na	Mn	O	K	Na	Mn	O	K	Na
	at.-%	at.-%	at.-%	at.-%	at.-%	at.-%	at.-%	at.-%	at.-%	at.-%	at.-%	at.-%	at.-%	at.-%	at.-%	at.-%
α-MnO_2-SF	34.30	61.47	4.13	—	35.64	60.19	4.17	—	31.84	64.32	3.84	—	35.37	60.55	4.08	—
MnO_2 activated	46.05	51.70	—	2.25	44.65	53.17	—	2.18	47.44	50.65	—	1.91	45.28	52.52	—	2.21
Mn_2O_3	49.12	50.88	—	—	49.60	50.40	—	—	49.92	50.08	—	—	49.38	50.62	—	—
Mn_3O_4	55.46	44.54	—	—	56.09	43.91	—	—	56.39	43.61	—	—	56.75	43.25	—	—

Section S18.4. XPS elemental analysis

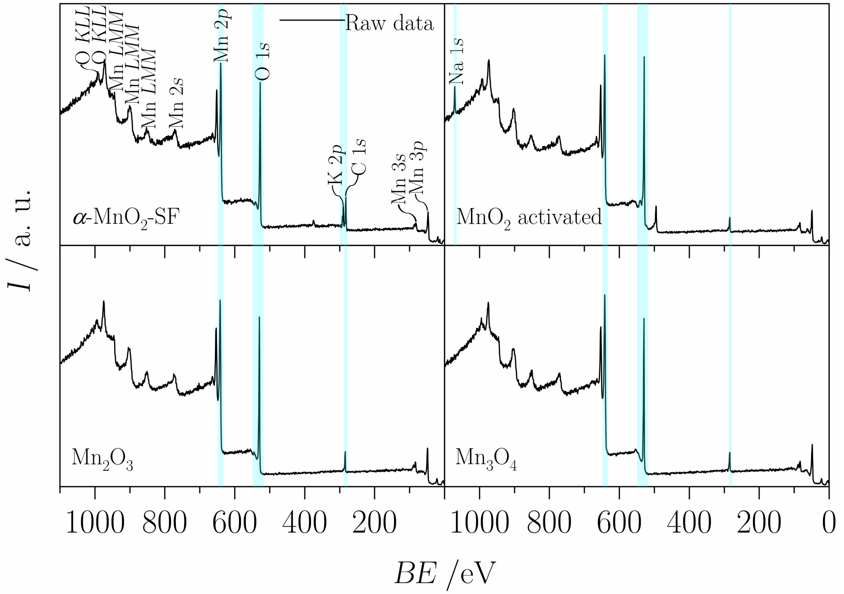

Figure S39. XP survey spectra of reference Mn oxides. Cyan areas highlight features used for the determination of elemental (surface) compositions. Elemental compositions were calculated from relative areas of fitted Mn $2p_{3/2}$, O 1*s*, K 2*p*, Ag $3d_{5/2}$, Na 1*s* and C 1*s* core-level photoemission spectra using CasaXPS processing software. α-MnO_2-SF and MnO_2 activated exhibit supplemental potassium (K) and sodium (Na), respectively.

Table S29. Summarized XPS elemental (surface) compositions of Mn, O, K and Na of reference Mn oxides based on relative areas of fitted Mn $2p_{3/2}$, O 1*s*, K 2*p* and Na 1*s* core-level photoemission spectra. C as derived from high-resolution C 1*s* core-level photoemission spectra was deducted as it is regarded a surface contamination due to air exposure during sample preparation.[7]

Mn oxide	Mn $2p_{3/2}$ at.-%	O 1*s* at.-%	K 2*p* at.-%	Na 1*s* at.-%
α-MnO_2-SF	30.59	60.37	9.04	—
MnO_2 activated	26.01	67.57	—	6.42
Mn_2O_3	35.35	64.65	—	—
Mn_3O_4	36.97	63.03	—	—

Section S18.5. Comparison of SEM-EDX and XPS elemental compositions

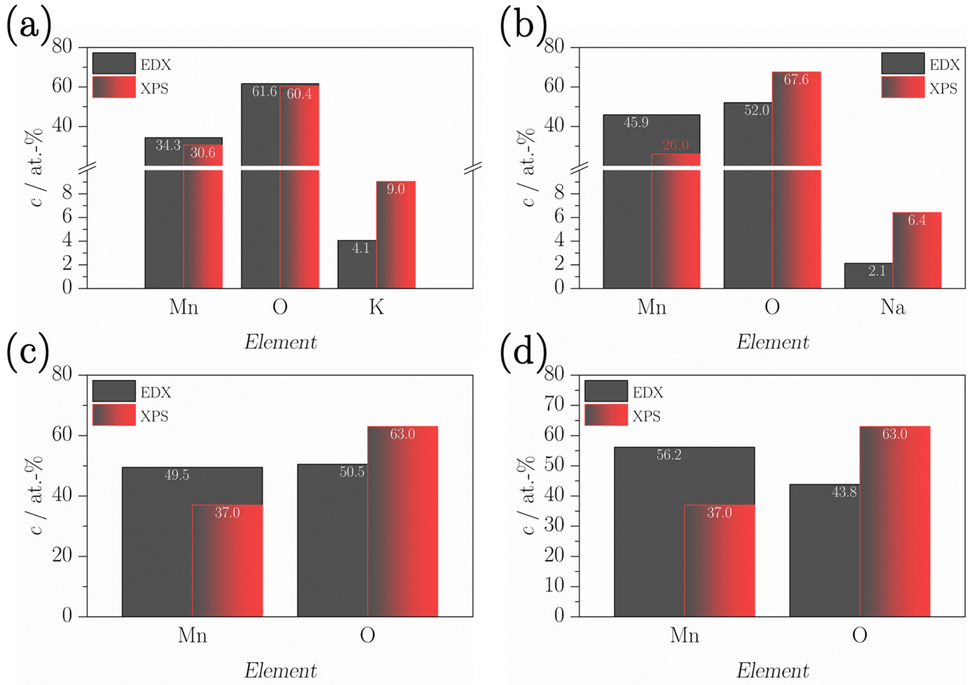

Figure S40. Summary of SEM-EDX (gray columns) and XPS (gray-red graded columns) elemental compositions of reference Mn oxides. (a) α-MnO_2-SF, (b) commercial MnO_2 activated, (c) commercial Mn_2O_3 and (d) commercial Mn_3O_4. Columns representing results from XPS are inserted into the gray columns of EDX in order to emphasize the different „penetration depths“ of both techniques.

α-MnO_2-SF demonstrate an elemental composition consisting of Mn, O and K. While the ratio of Mn and O is largely constant, less K content of 4.1 at.-% by EDX as compared to 9.0 at.-% detected by XPS reveals an increasing concentration gradient towards the outer of the agglomerates. Similar applies to commercial MnO_2 activated, but displays a significant Na content instead. Since it is commercially purchased, we suspect that Na most likely originates from a precursor used for the preparation. In case of commercial Mn_2O_3 and Mn_3O_4 both EDX and XPS merely detected Mn and O.

Section S18.6. N_2 adsorption-desorption measurements

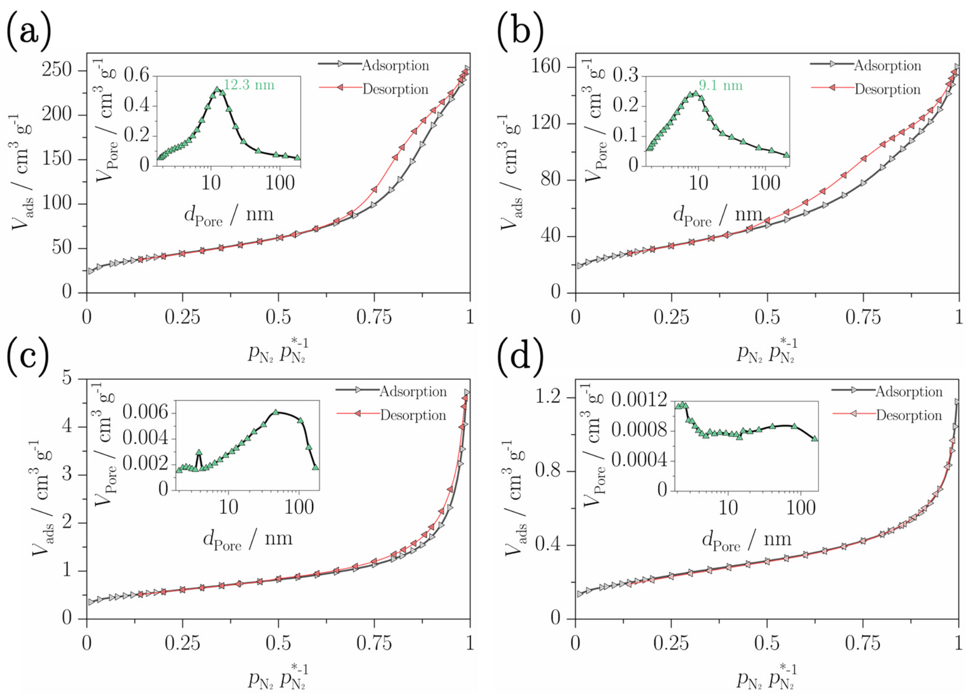

Figure S41. N_2 adsorption-desorption isotherms and Barrett-Joyner-Halenda (BJH) pore size distribution (PSD) curves (inset) of reference Mn oxides. (a) of α-MnO_2-SF, (b) commercial MnO_2 activated, (c) commercial Mn_2O_3 and (d) commercial Mn_3O_4.

Table S30. Summarized Brunauer, Emmett and Teller (BET) specific surface areas (BET *SA*), modal pore diameters (d_{Pore}) from BJH pore size distribution curves, BJH average pore diameters ($\bar{d}_{Pore}$) and BJH cumulative pore volumes (V_{Pore}) as obtained from N_2 adsorption-desorption measurements of reference Mn oxides.

Mn oxide	BET *SA*	d_{Pore}	$\bar{d}_{Pore}$	V_{Pore}
	$m^2\ g^{-1}$	nm	nm	$cm^3\ g^{-1}$
α-MnO_2-SF	149.9	12.3	9.0	0.4
MnO_2 activated	113.0	9.1	7.0	0,25
Mn_2O_3	2.1	—	—	—
Mn_3O_4	0.8	—	—	—

Adsorption branches of α-MnO_2-SF (**Figure S41a**) as well as commercial MnO_2 activated (**Figure S41b**) resemble a type II shape with regard to IUPAC classification, but hysteresis loops are of a H3 type usually given by non-rigid agglomerates, or loose assemblages, respectively, which is in good agreement with SEM images of both MnO_2. Moreover, broad pore size distributions (PSDs) typical of H3 type hysteresis could be observed for α-MnO_2-SF (**Figure S41a** inset, d_{Pore}=12.3 nm, $\bar{d}_{Pore}$=9.0 nm) and commercial MnO_2 activated (**Figure S41b** inset, d_{Pore}=9.1 nm, $\bar{d}_{Pore}$=7.0 nm). In contrast, isotherms of commercial Mn_2O_3 (**Figure S41c**) and Mn_3O_4 (**Figure S41d**) depict a type II shape, but slightly crossing over to a type III at low $p_{N_2}\, p_{N_2}^{*-1}$ with regard to IUPAC classification. In general, both type II and type III isotherms are indicative for non-porous, or macroporous materials. Hence, the minor hysteresis loop in case of Mn_2O_3, which likewise indicates mesoporous features, is in good agreement with its PSD (**Figure S41c** inset) exhibiting a bimodal distribution within the meso- and macroporous range.[36,38,58] In contrast, Mn_3O_4`s isotherms are completely reversible indicating non-porousity, that is, however, in good accordance with its inconclusive PSD (**Figure S41d** inset).[36,38,58] Nevertheless, we would like to expressly point out, for a precise analysis of macroporous features one should carry out, e.g., mercury porosimetry,[59] but this is beyond the scope of this study.

Section S19. Details on the thin-film rotating disk electrode (TF-RDE) set-up

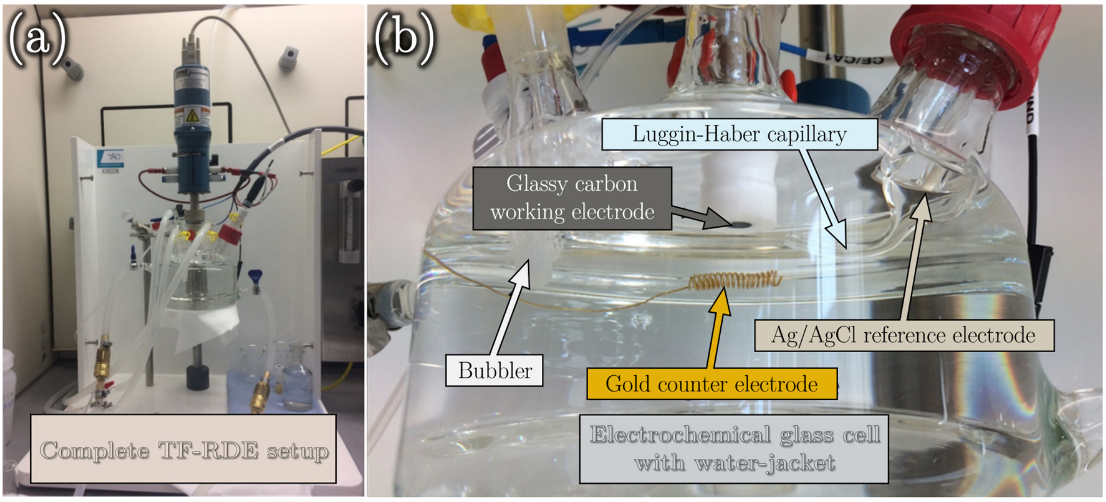

Figure S42. Thin-film rotating disk electrode (TF-RDE) set-up used for the evaluation of ORR electrocatalytic activities and electrochemically active surface areas (*ECSAs*). (a) Complete TF-RDE setup and (b) magnified in-house build water-jacketed glass cell showing the three-electrode configuration as describe in the experimental section of the manuscript, i.e., the glassy carbon (GC) disk working electrode, gold counter electrode and Ag/AgCl (sat. KCl) reference electrode mounted in an in-house built Luggin-Haber capillary.

Section S20. References

1 C. J. Humphreys, The Significance of Bragg's Law in Electron Diffraction and Microscopy, and Bragg's Second Law, *Acta Crystallogr., Sec. A: Found. Crystallogr.*, 2013, **69**, 45–50.

2 C. Tannous, Crystal Structure, X-Ray Diffraction and Oblique Geometry, *Eur. J. Phys.*, 2020, **41**, 15501.

3 A. E. Blagov, M. V. Dekapoltsev, M. V. Kovalchuk, V. V. Lider, Y. V. Pisarevsky and P. A. Prosekov, Lattice Parameter Local Determination for Trigonal, Hexagonal, and Tetragonal Crystal Systems Using Several Coplanar X-Ray Reflections, *Crystallogr. Rep.*, 2010, **55**, 1074–1078.

4 D. Fang, F. He, J. Xie and L. Xue, Calibration of Binding Energy Positions with C 1*s* for XPS Results, *J. Wuhan Univ. Technol.-Mat. Sci. Edit.*, 2020, **35**, 711–718.

5 G. Greczynski and L. Hultman, X-Ray Photoelectron Spectroscopy: Towards Reliable Binding Energy Referencing, *Prog. Mater. Sci.*, 2020, **107**, 100591.

6 S. Tougaard, Practical Guide to the Use of Backgrounds in Quantitative XPS, *J. Vac. Sci. Technol. A*, 2021, **39**, 11201.

7 A. Shchukarev and D. Korolkov, XPS Study of group IA carbonates, *Open Chem.*, 2004, **2**, 347–362.

8 D. Titus, E. J. J. Samuel and S. M. Roopan, Chapter 12 - Nanoparticle Characterization Techniques, In *Green Synthesis, Characterization and Applications of Nanoparticles*, First Edition, Ed. A. K. Shukla, S. Iravani, Elsevier, Amsterdam, Netherlands, 2019, 303–319.

9 I. Prencipe, D. Dellasega, A. Zani, D. Rizzo and M. Passoni, Energy Dispersive X-Ray Spectroscopy for Nanostructured Thin Film Density Evaluation, *Sci. Technol. Adv. Mater.,* 2015, **16**, 25007.

10 E. D. Giglio, N. Ditaranto and L. Sabbatini, 3. Polymer Surface Chemistry: Characterization by XPS, In *Polymer Surface Characterization*, Ed. L. Sabbatini, DE GRUYTER, Berlin, Boston, 2014, 73–111.

11 P. Leinweber, J. Kruse, C. Baum, M. Arcand, J. D. Knight, R. Farrell, K.-U. Eckhardt, K. Kiersch and G. Jandl, Advances in Understanding Organic Nitrogen Chemistry in Soils Using State-of-the-Art Analytical Techniques, *Adv. Agron.*, 2013, **119**, 83–151.

12 M. Kim, J.-H. Seo, D. Zhao, S.-C. Liu, K. Kim, K. Lim, W. Zhou, E. Waks and Z. Ma, Transferrable Single Crystalline 4H-SiC Nanomembranes, *J. Mater. Chem. C*, 2017, **5**, 264–268.

13 Y. Wu, Y. Lin and J. Xu, Synthesis of Ag-Ho, Ag-Sm, Ag-Zn, Ag-Cu, Ag-Cs, Ag-Zr, Ag-Er, Ag-Y and Ag-Co Metal Organic Nanoparticles for UV-Vis-NIR Wide-Range Bio-Tissue Imaging, *Photochem. Photobiol. Sci.*, 2019, **18**, 1081–1091.

14 A. Ganguly, S. Sharma, P. Papakonstantinou and J. Hamilton, Probing the Thermal Deoxygenation of Graphene Oxide Using High-Resolution In Situ X-Ray-Based Spectroscopies, *J. Phys. Chem. C*, 2011, **115**, 17009–17019.

15 V. Di Castro and G. Polzonetti, XPS Study of MnO Oxidation, *J. Electron Spectrosc. Relat. Phenom.*, 1989, **48**, 117–123.

16 M. Oku, K. Hirokawa and S. Ikeda, X-Ray Photoelectron Spectroscopy of Manganese-Oxygen Systems, *J. Electron Spectrosc. Relat. Phenom.*, 1975, **7**, 465–473.

17 R. Tholkappiyan, A. N. Naveen, K. Vishista and F. Hamed, Investigation on the Electrochemical Performance of Hausmannite Mn_3O_4 Nanoparticles by Ultrasonic Irradiation Assisted Co-Precipitation Method for Supercapacitor Electrodes, *J. Taibah Univ. Sci.*, 2018, **12**, 669–677.

18 C. Xu, S. Shi, Y. Sun, Y. Chen and F. Kang, Ultrathin Amorphous Manganese Dioxide Nanosheets Synthesized with Controllable Width, *Chem. Commun. (Cambridge, U. K.)*, 2013, **49**, 7331–7333.

19 F. Bohlooli, A. Yamatogi and S. Mori, Manganese Oxides/Carbon Nanowall Nanocomposite Electrode as an Efficient Non-Enzymatic Electrochemical Sensor for Hydrogen Peroxide, *Sens. Bio-Sens. Res.*, 2021, **31**, 100392.

20 A. S. Poyraz, J. Huang, S. Cheng, L. Wu, X. Tong, Y. Zhu, A. C. Marschilok, K. J. Takeuchi and E. S. Takeuchi, Tunnel Structured α-MnO_2 with Different Tunnel Cations (H^+, K^+, Ag^+) as Cathode Materials in Rechargeable Lithium Batteries: The Role of Tunnel Cation on Electrochemistry, *J. Electrochem. Soc.*, 2017, **164**, A1983-A1990.

21 A. S. Poyraz, J. Huang, S. Cheng, D. C. Bock, L. Wu, Y. Zhu, A. C. Marschilok, K. J. Takeuchi and E. S. Takeuchi, Effective Recycling of Manganese Oxide Cathodes for Lithium Based Batteries, *Green Chem.*, 2016, **18**, 3414–3421.

22 W. Yan, T. Ayvazian, J. Kim, Y. Liu, K. C. Donavan, W. Xing, Y. Yang, J. C. Hemminger and R. M. Penner, Mesoporous Manganese Oxide Nanowires for High-Capacity, High-Rate, Hybrid Electrical Energy Storage, *ACS Nano*, 2011, **5**, 8275–8287.

23 M. Chigane and M. Ishikawa, Manganese Oxide Thin Film Preparation by Potentiostatic Electrolyses and Electrochromism, *J. Electrochem. Soc.*, 2000, **147**, 2246.

24 V. P. Santos, O. S. G. P. Soares, J. J. W. Bakker, M. F. R. Pereira, J. J. M. Órfão, J. Gascon, F. Kapteijn and J. L. Figueiredo, Structural and Chemical Disorder of Cryptomelane Promoted by Alkali Doping: Influence on Catalytic Properties, *J. Catal.*, 2012, **293**, 165–174.

25 M. Toupin, T. Brousse and D. Bélanger, Charge Storage Mechanism of MnO_2 Electrode Used in Aqueous Electrochemical Capacitor, *Chem. Mater.*, 2004, **16**, 3184–3190.

26 V. R. Galakhov, M. Demeter, S. Bartkowski, M. Neumann, N. A. Ovechkina, E. Z. Kurmaev, N. I. Lobachevskaya, Y. M. Mukovskii, J. Mitchell and D. L. Ederer, Mn 3*s* Exchange Splitting in Mixed-Valence Manganites, *Phys. Rev. B*, 2002, **65**. 113102-1–113102-4.

27 E. S. Ilton, J. E. Post, P. J. Heaney, F. T. Ling and S. N. Kerisit, XPS Determination of Mn Oxidation States in Mn (Hydr)Oxides, *Appl. Surf. Sci.*, 2016, **366**, 475–485.

28 Z. Ye, J.-M. Giraudon, N. de Geyter, R. Morent and J.-F. Lamonier, The Design of MnO_x Based Catalyst in Post-Plasma Catalysis Configuration for Toluene Abatement, *Catalysts*, 2018, **8**, 91.

29 R. Cao, L. Li, P. Zhang, L. Gao and S. Rong, Regulating Oxygen Vacancies in Ultrathin δ-MnO_2 Nanosheets with Superior Activity for Gaseous Ozone Decomposition, *Environ. Sci.: Nano*, 2021, **8**, 1628–1641.

30 J. Luo, Q. Zhang, J. Garcia-Martinez and S. L. Suib, Adsorptive and Acidic Properties, Reversible Lattice Oxygen Evolution, and Catalytic Mechanism of Cryptomelane-Type Manganese Oxides as Oxidation Catalysts, *J. Am. Chem. Soc.*, 2008, **130**, 3198–3207.

31 G. Zhu, J. Zhu, W. Jiang, Z. Zhang, J. Wang, Y. Zhu and Q. Zhang, Surface Oxygen Vacancy Induced α-MnO_2 Nanofiber for Highly Efficient Ozone Elimination, *Appl. Catal., B*, 2017, **209**, 729–737.

32 J. Zeng, H. Xie, Z. Liu, X. Liu, G. Zhou and Y. Jiang, Oxygen Vacancy Induced MnO_2 Catalysts for Efficient Toluene Catalytic Oxidation, *Catal. Sci. Technol.*, 2021, **11**, 6708–6723.

33 J. A. Dawson, H. Chen and I. Tanaka, First-Principles Calculations of Oxygen Vacancy Formation and Metallic Behavior at a β-MnO_2 Grain Boundary, *ACS Appl. Mater. Interfaces*, 2015, **7**, 1726–1734.

34 J. Hou, Y. Li, L. Liu, L. Ren and X. Zhao, Effect of Giant Oxygen Vacancy Defects on the Catalytic Oxidation of OMS-2 Nanorods, *J. Mater. Chem. A*, 2013, **1**, 6736.

35 J. Garcia-Martinez, C. Xiao, K. A. Cychosz, K. Li, W. Wan, X. Zou and M. Thommes, Evidence of Intracrystalline Mesostructured Porosity in Zeolites by Advanced Gas Sorption, Electron Tomography and Rotation Electron Diffraction, *ChemCatChem*, 2014, **6**, 3110–3115.

36 M. Thommes, K. Kaneko, A. V. Neimark, J. P. Olivier, F. Rodriguez-Reinoso, J. Rouquerol and K. S.W. Sing, Physisorption of Gases, with Special Reference to the Evaluation of Surface Area and Pore Size Distribution (IUPAC Technical Report), *Pure Appl. Chem.*, 2015, **87**, 1051–1069.

37 K. A. Cychosz, R. Guillet-Nicolas, J. García-Martínez and M. Thommes, Recent Advances in the Textural Characterization of Hierarchically Structured Nanoporous Materials, *Chem. Soc. Rev.*, 2017, **46**, 389–414.

38 M. Thommes, R. Köhn and M. Fröba, Sorption and Pore Condensation Behavior of Pure Fluids in Mesoporous MCM-48 Silica, MCM-41 Silica, SBA-15 Silica and Controlled-Pore Glass at Temperatures Above and Below the Bulk Triple Point, *Appl. Surf. Sci.*, 2002, **196**, 239–249.

39 T. Horikawa, D. D. Do and D. Nicholson, Capillary Condensation of Adsorbates in Porous Materials, *Adv. Colloid Interface Sci.*, 2011, **169**, 40–58.

40 M. F. Fink, J. Eckhardt, P. Khadke, T. Gerdes and C. Roth, Bifunctional α-MnO_2 and Co_3O_4 Catalyst for Oxygen Electrocatalysis in Alkaline Solution, *ChemElectroChem*, 2020, **7**, 4822–4836.

41 L. Feng, Z. Xuan, H. Zhao, Y. Bai, J. Guo, C.-W. Su and X. Chen, MnO_2 Prepared by Hydrothermal Method and Electrochemical Performance as Anode for Lithium-Ion Battery, *Nanoscale Res. Lett.*, 2014, **9**, 290.

42 A. A. Hlaing and P. P. Win, The Synthesis of α-MnO_2 Nanorods Using Hydrothermal Homogeneous Precipitation, *Adv. Nat. Sci: Nanosci. Nanotechnol.*, 2012, **3**, 25001.

43 Y.-J. Shih, P.-Y. Cheng, B. O. Ariyanto and Y.-H. Huang, Electrochemical Oxidation of Carboxylic Acids in the Presence of Manganese Chloride, *J. Electrochem. Soc.*, 2013, **160**, H681-H686.

44 C.-H. Kim, Z. Akase, L. Zhang, A. H. Heuer, A. E. Newman and P. J. Hughes, The Structure and Ordering of ε-MnO_2, *J. Solid State Chem.,* 2006, **179**, 753–774.

45 Z. Dai, X. Yu, C. Huang, M. Li, J. Su, Y. Guo, H. Xu and Q. Ke, Nanocrystalline MnO_2 on an Activated Carbon Fiber for Catalytic Formaldehyde Removal, *RSC Adv.*, 2016, **6**, 97022–97029.

46 Y. Zhao, A Synthesis Technology of Honeycomb-Like Structure MnO_2 from Low Grade Manganese Ore, *MOJ Appl. Bionics Biomech.*, 2018, **2**. 57–60.

47 A. Biswal, B. Chandra Tripathy, K. Sanjay, T. Subbaiah and M. Minakshi, Electrolytic Manganese Dioxide (EMD): A Perspective on Worldwide Production, Reserves and Its Role in Electrochemistry, *RSC Adv.*, 2015, **5**, 58255–58283.

48 S. Noventa, D. Rowe and T. Galloway, Mitigating Effect of Organic Matter on the In Vivo Toxicity of Metal Oxide Nanoparticles in the Marine Environment, *Environ. Sci.: Nano*, 2018, **5**, 1764–1777.

49 G. V. Sokolsky, S. V. Ivanov, N. D. Ivanova, Y.I. Boldurev, O. V. Kobulinskaya and M. V. Demchenko, Cobalt Additives Influence on Phase Composition and Defect Structure of Manganese Dioxide Prepared from Fluorine Containing Electrolytes, *Acta Phys. Pol. A*, 2010, **117**, 86–90.

50 Y. Chabre and J. Pannetier, Structural and Electrochemical Properties of the Proton / γ-MnO_2 System, *Prog. Solid State Chem.*, 1995, **23**, 1–130.

51 J. Attenburrow, A. F. B. Cameron, J. H. Chapman, R. M. Evans, B. A. Hems, A. B. A. Jansen and T. Walker, 194. A Synthesis of Vitamin a from Cyclohexanone, *J. Chem. Soc.*, 1952, 1094–1111.

52 S. Zhan, D. Zhu, M. Qiu, H. Yu and Y. Li, Highly Efficient Removal of NO with Ordered Mesoporous Manganese Oxide at Low Temperature, *RSC Adv.*, 2015, **5**, 29353–29361.

53 L. V. Stebounova, N. I. Gonzalez-Pech, T. M. Peters and V. H. Grassian, Physicochemical Properties of Air Discharge-Generated Manganese Oxide Nanoparticles: Comparison to Welding Fumes, *Environ. Sci. Nano*, 2018, **2018**, 696–707.

54 A. M. Hashem, S. M. Abbas, X. Hou, A. E. Eid and A. E. Abdel-Ghany, Facile One Step Synthesis Method of Spinel $LiMn_2O_4$ Cathode Material for Lithium Batteries, *Heliyon*, 2019, **5**, e02027.

55 K. A. M. Ahmed and K. Huang, Formation of Mn_3O_4 Nanobelts through the Solvothermal Process and Their Photocatalytic Property, *Arabian J. Chem.*, 2019, **12**, 429–439.

56 M. S. Osgouei, N. Kamrani and M. Khatamian, Improved Visible-Light Photocatalytic Activity of Mn_3O_4-Based Photocatalysts in Removal of Methylene Orange, *Mater. Chem. Phys.*, 2020, **239**, 122108–122118.

57 T. Peng, L. Xu and H. Chen, Preparation and Characterization of High Specific Surface Area Mn_3O_4 from Electrolytic Manganese Residue, *Open Chem.*, 2010, **8**, 1059–1068.

58 M. Thommes, Physical Adsorption Characterization of Nanoporous Materials, *Chemie Ing. Tech.*, 2010, **82**, 1059–1073.

59 J. Rouquerol, G. Baron, R. Denoyel, H. Giesche, J. Groen, P. Klobes, P. Levitz, A. V. Neimark, S. Rigby, R. Skudas, K. Sing, M. Thommes and K. Unger, Liquid Intrusion and Alternative Methods for the Characterization of Macroporous Materials (IUPAC Technical Report), *Pure Appl. Chem.,* 2011, **84**, 107–136.